https://doi.org/10.5194/egusphere-2026-3879
Preprint. Discussion started: 27 July 2026

Seasonal variability in methane emissions from the Yangtze River Delta revealed by a high-resolution atmospheric inversion

Mengrong Lu[1], Huilin Chen[2,3]*, Xun Zhang[2], Xuguang Chi[2], Chong Wei[4], Shuangxi Fang[5,6], Fenjuan Wang[7], Eleftherios Ioannidis[8], Friedemann Reum[9], Xinlu Wang[10,11,12], Prajal Pradhan[1,13], Wouter Peters[14], Klaus Hubacek[1], Sander Houweling[15,16]

[1]Integrated Research on Energy, Environment and Society (IREES), Energy and Sustainability Research Institute Groningen, University of Groningen, Groningen, 9747 AG, the Netherlands

[2]Joint International Research Laboratory of Atmospheric and Earth System Sciences, School of Atmospheric Sciences, Nanjing University, Nanjing, China

[3]Center for Isotope Research (CIO), Energy and Sustainability Research Institute Groningen (ESRIG), University of Groningen, Groningen, the Netherlands

[4]Center for Advanced Energy Systems and Equipment, Shanghai Advanced Research Institute, Chinese Academy of Sciences, Shanghai 201210, China

[5]Zhejiang Carbon Neutral Innovation Institute & Zhejiang International Cooperation Base for Science and Technology on Carbon Emission Reduction and Monitoring, Zhejiang University of Technology, Hangzhou 310014, China

[6]Collaborative Innovation Center on Forecast and Evaluation of Meteorological Disasters (CIC-FEMD), Nanjing University of Information Science & Technology, Nanjing 210044, China

[7]Satellite Observation Center, Earth System Division, National Institute for Environmental Studies (NIES), Japan

[8]Research & Development Satellite Observations, Royal Netherlands Meteorological Institute (KNMI), De Bilt, the Netherlands

[9]Deutsches Zentrum für Luft- und Raumfahrt e.V., Institut für Physik der Atmosphäre, Oberpfaffenhofen, Germany

[10]Key Laboratory of Coastal Environment and Resources of Zhejiang Province, School of Engineering, Westlake University, Hangzhou 310030, Zhejiang, China

[11]Institute of Advanced Technology, Westlake Institute for Advanced Study, Hangzhou 310024, Zhejiang, China

[12]College of Environmental and Resource Sciences, Zhejiang University, Hangzhou 310058, Zhejiang, China

[13]Potsdam Institute of Climate Impact Research (PIK), Member of Leibniz Association, Potsdam 14473, Germany

[14]Meteorology and Air Quality group, Wageningen University, Wageningen, the Netherlands

[15]Department of Earth Sciences, Vrije Universiteit, Amsterdam, the Netherlands

[16]SRON, Netherlands Institute for Space Research, Leiden, the Netherlands

Correspondence to: Huilin Chen (huilin.chen@nju.edu.cn, huilin.chen@rug.nl)

https://doi.org/10.5194/egusphere-2026-3879
Preprint. Discussion started: 27 July 2026

Abstract. Accurate methane (CH_4) emission estimates are essential for attributing regional CH_4 sources and quantifying their spatial and temporal variability, particularly in high-emission regions of China under stringent mitigation policies. Here, we apply CTDAS-WRF, a regional inversion framework that couples the CarbonTracker Data Assimilation Shell (CTDAS) with WRF-Chem, to quantify CH_4 emissions over East Asia. Through Observing System Simulation Experiments (OSSEs), we find that the system can recover ~61% of the imposed prior-to-truth adjustment in the Yangtze River Delta (YRD), 68% in South Korea, and 93% in northern Japan, indicating good performance in observation-rich regions. Using a composite prior for anthropogenic emissions based on EDGAR_2024 and CAMS v6.2, the 2022 inversion yields total posterior emissions of 7.53±0.09 Tg yr^{-1} in the YRD, which is 11.0% lower than the prior (8.46 Tg yr^{-1}). Prior anthropogenic emissions are overestimated by 12.7% (0.9 Tg yr^{-1}), while prior natural emissions are also higher by 0.03 Tg yr^{-1}. Daily posterior emissions exhibit a much stronger seasonal cycle and peak in summer, with natural sources and rice cultivation dominating the summertime underestimate in the prior. Independent evaluation at in situ station further supports the posterior improvement, with the daily mean absolute error reduced by 3.4 ppb (11.0%) relative to the prior simulation. This work highlights the importance of accounting for seasonal variability in YRD emissions and provides a basis for future inversions that integrate in situ and satellite observations to better constrain the CH_4 budget of East Asia.

1 Introduction

Methane (CH_4) is the second most impactful anthropogenic greenhouse gas. The atmospheric CH_4 concentration growth rate has accelerated markedly over the past two decades, underscoring its increasing role in near-term climate forcing (Lan et al., 2026; Saunois et al., 2025). As a major contributor to greenhouse-gas radiative forcing, CH_4 has become an important target of global mitigation efforts, as illustrated by the Global Methane Pledge and the growing emphasis on CH_4 abatement under the Paris Agreement. (GMP, 2023; Kirschke et al., 2013; Saunois et al., 2020; Stocker, 2013). China has been the world's largest anthropogenic CH_4 emitter since the 2000s, with more than 75 % of its emissions from human activities and substantial growth driven by rapid economic development, urbanization, and increasing waste generation (Cai et al., 2018; Crippa et al., 2023; Stavert et al., 2022; Sun et al., 2026; Yin et al., 2021). Major sources include coal mining in resource-rich provinces such as Shanxi, as well

https://doi.org/10.5194/egusphere-2026-3879
Preprint. Discussion started: 27 July 2026

as rice cultivation, livestock, and waste treatment in densely populated and economically developed regions such as the Yangtze River Delta (YRD) and Pearl River Delta (PRD) (Ai et al., 2024; Zhang et al., 2022). In response, China has introduced the Methane Emission Control Action Plan to strengthen sector-specific mitigation, including coal mine gas utilization and manure resource use (MECAP, 2023). In this context, accurately quantifying the spatiotemporal distribution of regional CH_4 emissions in China is essential for tracking emission dynamics, evaluating mitigation policies, and supporting effective climate action.

Greenhouse gas emission inventories are derived from bottom-up approaches using activity data and emission factors (Sheng et al., 2019). These inventories are now highly detailed, as evidenced by global datasets such as EDGAR (Emissions Database for Global Atmospheric Research; Crippa et al., 2024) and CAMS (Copernicus Atmosphere Monitoring Service). In China, high-resolution CH_4 inventories have been developed, which often focus on a specific source sector such as coal mining (Chen et al., 2024; Liu et al., 2024), rice cultivation (Wang et al., 2023), livestock (Wang et al., 2024), and wastewater (Liu et al., 2024). However, substantial discrepancies remain among available CH_4 emission inventories. These differences arise from inconsistent source definitions, sectoral aggregation, activity data, and emission factor assumptions across inventories, which are particularly pronounced for agriculture, waste, and fossil-fuel-related sources (Khanna et al., 2024; Saunois et al., 2025). Top-down atmospheric inverse studies are essential for further investigating and reducing these uncertainties. By relating atmospheric observations to surface fluxes through chemical transport models (CTMs), top-down inversions provide an independent framework for evaluating and reconciling differences among emission inventories (Worden et al., 2022).

In observation-dense regions (e.g., the United States and Europe), multiple regional inversion systems have been developed and applied (Nesser et al., 2024; Thompson et al., 2021; Tsuruta et al., 2025). These systems leverage Bayesian inversion frameworks, along with atmospheric CTMs, to successfully integrate satellite observations with continuous ground-based (stations, towers, and ships) and aircraft measurements (Lu et al., 2022; Sheng et al., 2018). They optimize multi-source emissions based on atmospheric concentrations, markedly reducing inventory uncertainties. For example, Estrada et al. (2025) presented a user-friendly inversion platform, IMI 2.0 (Integrated Methane Inversion version 2), that combines TROPOMI (launched in 2017; ~5.5×7 km since August 2019; Lorente et al., 2021) and

https://doi.org/10.5194/egusphere-2026-3879
Preprint. Discussion started: 27 July 2026

GOSAT (launched in 2009; pixel size ~10 km; Kuze et al., 2016) datasets to infer 2023 United States CH_4 emissions on a 25 km × 25 km grid, yielding estimates consistent with those from contemporary inversions. Steiner et al. (2024) and Ioannidis et al. (2026) used ground-based observations and the CarbonTracker Data Assimilation Shell (CTDAS), coupled to the CTMs (ICON-ART and WRF-Chem), to optimize three-year national totals and anthropogenic CH_4 fluxes for Europe.

Satellite datasets have supported the development of inversion studies in regions with limited in situ coverage, such as China (He et al., 2024; Liang et al., 2023, 2024; Qu et al., 2021; Zhang et al., 2022). However, satellite-based inversions face several issues: (i) uneven spatial coverage and limited temporal continuity, limiting applications that require high temporal resolution (Chen et al., 2022); and (ii) strong constraints on column abundances (XCH_4) but weaker sensitivity to surface emissions (Turner et al., 2018). In contrast, ground-based observations provide continuous temporal coverage and are therefore particularly valuable for constraining seasonal changes in emissions. Moreover, Steiner et al. (2024) report regional discrepancies between inversions constrained by satellite observations and those constrained by different surface measurement networks. This motivates cross-dataset intercomparisons to evaluate the robustness of regional inversions under different observational constraints and to interpret any inconsistencies.

Compared with inventories or approaches based on prescribed scaling factors, observation-constrained inversions may provide additional constraints on temporal emission variability, especially where continuous atmospheric observations are available (Hu et al., 2023, 2026; Feng et al., 2025). Previous studies have extensively discussed the seasonal characteristics of CH_4 emissions. Feng et al. (2025) identify a winter-low and summer-high pattern in CH_4 emissions, with stronger summer increases in rice cultivation and waste emissions, but their analysis focuses mainly on Shanxi and assumes fixed variability in natural emissions. Hu et al. (2023, 2026) partly address this gap by using tower observations to constrain CH_4 emissions over the YRD, revealing pronounced seasonal variability and substantial biases in the prior regional emission pattern. However, most of these studies use Lagrangian approaches, which are efficient for resolving city-scale, tower-based near-field footprints but provide limited constraint on larger regions such as the YRD (Hu et al., 2026). Therefore, a regional Eulerian inversion framework is still needed to evaluate emission seasonality across the YRD.

CTDAS-WRF (Reum et al., 2020) is an Ensemble Kalman Filter (EnKF)-based regional inversion system

https://doi.org/10.5194/egusphere-2026-3879
Preprint. Discussion started: 27 July 2026

that couples the CTDAS inversion framework (Peters et al., 2005; van der Laan-Luijkx et al., 2017) with the widely used regional chemical transport model WRF-Chem (Skamarock et al., 2019). In this study, we apply CTDAS-WRF over East Asia, a major global CH_4 hotspot (Thompson et al., 2015), to quantify CH_4 emissions at high spatial and temporal resolution. We aim to (1) identify optimal parameterizations through a series of sensitivity tests conducted within an Observing System Simulation Experiment (OSSE) framework (Sect. 3.1), (2) analyze and evaluate the full-year 2022 inversion results based on real in situ data, with emphasis on the Yangtze River Delta (YRD) in China (Sect. 3.2), and (3) assess the system's credibility and robustness through cross-comparison with existing inversions and inventories, and validation against independent observations (Sect. 3.3). We summarize the main conclusions and implications in Sect. 4. The results improve the spatial and temporal characterization of CH_4 emissions relative to the prior, particularly in the YRD, as reflected by the better agreement with independent observations, and thereby strengthen the attribution of regional and sectoral emissions and our understanding of the CH_4 budget in this key source region of East Asia.

2 Methodology

2.1 Chemical transport model: WRF-Chem

The CTM used in this study is the Weather Research and Forecasting model with Chemistry (WRF-Chem) version 4.5.2 (Grell et al., 2005; Skamarock and Klemp, 2008), developed by the National Center for Atmospheric Research (NCAR). The greenhouse gas module (WRF-GHG), which has been officially integrated into WRF-Chem (Beck et al., 2011; Callewaert et al., 2024) since version 3.4, simulates passive tracer transport driven by gridded fluxes from, for example, sector-specific emission inventories, and has been widely applied in regional inverse studies (Pillai et al., 2016; Vara-Vela et al., 2023). These fluxes are translated into three-dimensional atmospheric mixing ratio fields through Eulerian transport, with initial and boundary concentrations and flux-driven enhancements represented by tracer variables (Vara-Vela et al., 2023). All trace gases are treated as passive tracers that are transported using the WRF simulated meteorology driven by ERA5 meteorological fields with 0.25° spatial resolution and hourly temporal resolution (Hersbach et al., 2023a, b). Spectral nudging is activated to optimize the simulation (Lai and Gan, 2025). Details of the key WRF-Chem physical schemes, model configurations, and corresponding references are provided in Table S1. To represent the ensemble distribution during online transport, we add 100 tracers to the WRF tracer list, with one tracer assigned to each EnKF ensemble

https://doi.org/10.5194/egusphere-2026-3879
Preprint. Discussion started: 27 July 2026

member. The formulation of the state vector, including the ensemble construction and background parameters, is described in Sect. 2.2.

2.1.1 Study region

Our study domain is configured using a Lambert conformal projection and encompasses most of China, North Korea, South Korea, Japan, and parts of Mongolia, Vietnam, the Philippines, and Russia (Fig. 1a). The simulation uses a two-way nested domain setup. The parent domain (D01) has 138 × 138 grid cells (longitude × latitude) at a 27 km resolution. The nested domain (D02) is centered over the YRD, encompassing Shanghai and the provinces of Jiangsu, Zhejiang, and Anhui, with 108 × 111 grid cells at a 9 km resolution. Vertically, the model is configured with 50 layers up to 50 hPa (Table S1).

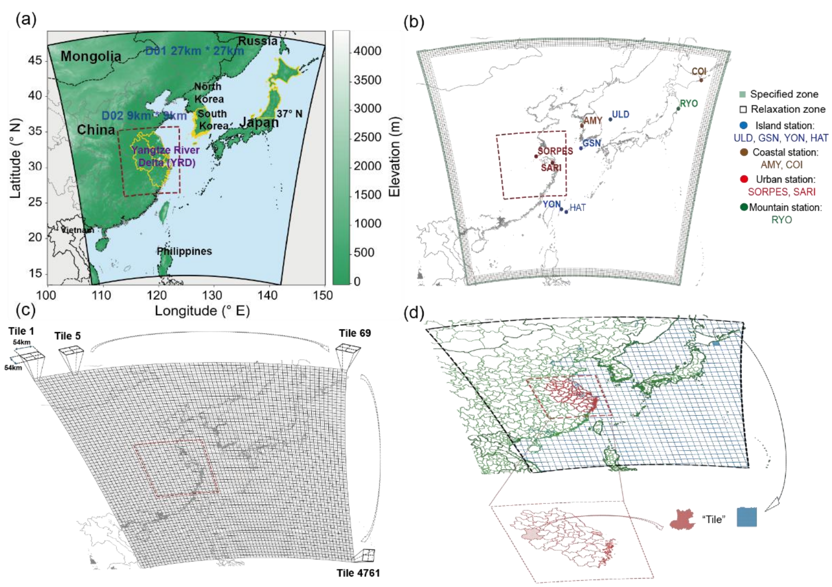

Figure 1: Study domain for the regional inversions. (a) WRF domain and the terrain elevation (parent domain D01, nested domain D02); (b) location of the stations used in the inversion (Sect. 2.4) and the boundary zones; (c) schematic definition of "tile" as an independent state-vector element in the parent domain; (d) region-based aggregation of the state vector over land and ocean used in a sensitivity test (Sect. 2.3.1). The elevation data is from Danielson and Gesch (2011).

2.1.2 Initial and boundary conditions

For the initial and lateral background fields of CH_4 concentrations, the initial value is used only in the first simulation window; in subsequent windows, the initial condition is taken from the last time step of the previous window. For the boundary conditions, we use a five-grid boundary zone composed of a

https://doi.org/10.5194/egusphere-2026-3879
Preprint. Discussion started: 27 July 2026

specified zone and a relaxation zone, where the parent-domain values are progressively relaxed toward the global fields (Fig. 1b, Wong et al., 2012).

Initial and boundary conditions are taken from the CAMS global inversion-optimized greenhouse-gas concentration, assimilated using satellite and ground-based observations, and available from the Copernicus Atmosphere Data Store (Bergamaschi et al., 2013). This product (v24r1) provides global gridded background CH_4 dry-air mole fractions at 1° × 1° spatial and 6-hour temporal resolution.

2.1.3 Prior flux

As summarized in Table 1, we use the EDGAR_2024 (European Commission, JRC, and IEA, 2024) and CAMS global emission inventories (Granier et al., 2019). EDGAR_2024 was the latest available release of the EDGAR inventory at the start of the experiments, providing annual emissions for 23 source sectors and monthly emissions for eight sectors on a 0.1° × 0.1° grid (Crippa et al., 2024); EDGAR_2025 (Crippa et al., 2025) was released later, on 1 October 2025. CAMS-GLOB-ANT v6.2 (CAMS v6.2; Soulie et al., 2024) is the latest CAMS global anthropogenic inventory and is constructed using multiple EDGAR releases (versions 4.3.2, 5.0, 6.0, and 7.0), the Community Emissions Data System (CEDS) datasets and the Regional Emission inventory in ASia (REAS) datasets.

During our inventory intercomparison over East Asia, we find that the agriculture and waste sectors in EDGAR_2024 show large differences in spatial patterns and peak magnitudes relative to earlier EDGAR releases, particularly EDGAR v6.0. In the livestock component of the agriculture sector, local peak values in EDGAR_2024 and EDGAR v8.0 (Crippa et al., 2023) exceed those in EDGAR v6.0 by more than two orders of magnitude. We also find substantial spatial redistribution in the waste sector relative to EDGAR v6.0, including a hotspot near 35.0°N, 118.2°E that is not prominent in the earlier release. These pronounced differences suggest substantial uncertainty in these sectoral fields for our study region. To avoid relying on inventory components with large inter-release discrepancies, we adopt a conservative hybrid approach and replace the EDGAR agriculture and waste sectors with the corresponding CAMS v6.2 categories, namely swd (solid waste and wastewater), agl (livestock), awb (agricultural waste burning), and ags (agricultural soils). For the other sectors, we use EDGAR_2024 rather than CAMS v6.2 because it provides the most recent gridded sectoral inventory used to represent the remaining anthropogenic sources in our experiments. Both CAMS and EDGAR provide high spatial resolution (0.1° × 0.1°), which is well suited to our high-resolution modeling framework. Although China-specific high-

https://doi.org/10.5194/egusphere-2026-3879
Preprint. Discussion started: 27 July 2026

resolution inventories such as PKU-CH_4 v2 (Liu et al., 2021; Peng et al., 2016) and CHN-CH4 (Guo et al., 2025) better represent activity information, CAMS and EDGAR are updated more frequently and with shorter release lags. Accordingly, we use the combined CAMS v6.2 and EDGAR_2024 inventory to supply up-to-date anthropogenic emissions.

Emissions from biomass burning are derived from the Global Fire Assimilation System (GFAS, Kaiser et al., 2012) dataset, which provides data at a spatial resolution of 0.1°. Natural fluxes considered in this study include emissions from wetlands, geological sources (such as hydrocarbon macro-seeps, mud volcanoes, diffuse micro-seepage, and geothermal activity), oceans, termites, inland water systems (including lakes, reservoirs, rivers, streams, and estuaries), as well as CH_4 uptake by soils (soil sink). Wetland emissions are calculated using the Earth Observation SIMulator (LPJ-EOSIM) version of the Lund-Potsdam-Jena Dynamic Global Vegetation Model (LPJ-DGVM). This open-access NASA-sponsored dataset provides daily wetland CH_4 fluxes at a spatial resolution of 0.5° × 0.5° (Colligan et al., 2024). Soil CH_4 uptake fluxes are derived from the Vegetation Integrative Simulator for Trace gases (VISIT version 2023.2, Ito, 2021). As VISIT provides data only for 2012–2021, fluxes through January 2023 are extrapolated using the 2012–2021 mean for each corresponding month. All other natural fluxes are derived from the climatological estimates of Saunois et al. (2020) and the corresponding contributors, using the reorganized versions provided by Wang et al. (2025) and Ito (2021). In our analysis, all flux sectors are allocated to seven categories, denoted as "$E_{CH4\_proc\_1}$" to "$E_{CH4\_proc\_6}$" and "*E_FIX*", as shown in Table 1. Note that *E_FIX* includes non-optimized fluxes including the soil sink and oceanic fluxes.

https://doi.org/10.5194/egusphere-2026-3879
Preprint. Discussion started: 27 July 2026

Table 1: Prior fluxes.

Categories (IPCC 2006 category; IPCC, 2006)				Data source	Re-categorization	Resolution	Time period	Prior uncertainty
Anthropogenic flux	Agriculture	Rice cultivation	Agricultural waste burning (3C1b)	CAMS v6.2	$E_{CH4\_proc\_1}$	0.1° × 0.1°/ monthly	2021–2023	0.3
			Agricultural soils (3C2+3C3+3C4+3C7)			0.1° × 0.1°/ monthly	2021–2023	
		Livestock	Enteric fermentation (3A1)		$E_{CH4\_proc\_5}$	0.1° × 0.1°/ monthly	2021–2023	0.3
			Manure management (3A2)					
	Waste	Waste water handling, solid waste landfills and solid waste incineration (4)			$E_{CH4\_proc\_3}$	0.1° × 0.1°/ monthly	2021–2023	0.3
	Energy for buildings (1A4+1A5), industrial combustion (1A2), industrial processes (2), power industry (1A1), transport (1A3)			EDGAR_2024	$E_{CH4\_proc\_6}$ (the "Other" sector)	0.1° × 0.1°/ monthly	2021–2023	0.3
	Fuel exploitation (1A1b+1A1c+1A5biii+1B+1B2+5B)				$E_{CH4\_proc\_4}$	0.1° × 0.1°/ monthly	2021–2023	0.4
Biomass burning emission	Dry matter burnt and biomass burning emissions			GFAS	$E_{CH4\_proc\_2}$ (the "Natural" sector)	0.1° × 0.1°/daily	2021–2023	0.5
Natural flux	wetland			LPJ-EOSIM L2		0.5° × 0.5°/daily	2021–2023	
	Termite (Saunois et al., 2020), freshwater (Stavert et al., 2022), geological (Etiope et al., 2019)			Wang et al. (2025)		0.1° × 0.1°/ monthly	Climatological map	
	Soil sink (Ito, 2021), ocean (Weber et al., 2019)			VISIT (Ito, 2021), Saunois et al. (2020)	*E_FIX* (not optimized)	0.1° × 0.1°/ monthly	For soil sink: 10-year average value; for ocean: climatological map	

https://doi.org/10.5194/egusphere-2026-3879
Preprint. Discussion started: 27 July 2026

2.2 Inversion framework: CarbonTracker Data Assimilation Shell (CTDAS)

2.2.1 Optimization scheme

The CTDAS-WRF system applies an Ensemble Kalman Filter (EnKF) to simultaneously optimize CH_4 fluxes and background parameters within a fixed assimilation window (Peters et al., 2005; He et al., 2018; van der Laan-Luijkx et al., 2017; Steiner et al., 2024). The state vector includes surface CH_4 flux scaling factors and eight background parameters. The observation operator is provided by WRF-Chem, which maps the state vector to observation space by sampling simulated CH_4 mole fractions at the observation times and locations. Prior uncertainty is represented by an ensemble of 100 members, in which the first member is set equal to the mean state and the remaining members represent perturbations around it. The full EnKF formulation is provided in Appendix A.

In this study, CTDAS is configured with two lags, so that each assimilation cycle simultaneously constrains two consecutive time windows (Fig. 2). During each cycle, WRF-Chem is first run with the current state vector for both lags, and the simulated CH_4 concentrations are sampled at the observation times and locations. The sampled observations are then assimilated to update the state vector and the associated flux scaling factors. This is followed by an advance step, in which lag 0 (window 1) is rerun with the optimized posterior fluxes. The resulting ensemble-mean three-dimensional CH_4 concentration field is then assigned to all ensemble members to initialize the next cycle. At the beginning of the inversion, prior flux scaling factors are set to 1. In subsequent cycles, the time period retained within the lagged assimilation window (i.e., window 2', Fig. 2) inherits the optimized posterior state from the previous cycle, while the newly entered time period (i.e., window 3) is initialized as a new prior ensemble (λ_3^b = 1). Thus, except for the first cycle (10–19 December 2021), each optimization window is initialized using information from the optimized posterior fluxes of the preceding cycle. The optimized scaling factors, $\lambda^a(r,t)$ are then applied to the prior emissions to obtain the posterior fluxes, as described in Eq. (1):

$$F^a(r,t) = \sum_{k=1}^{6} \lambda^a_{proc\_k}(r,t) \cdot F_k\,(r,t) + F_{fix}(r,t), \tag{1}$$

where F denotes the total CH_4 flux, r represents the tile index (Fig. 1c), t represents the time step, k indexes the emission category, ranging from 1 to 6 (Table 1), the superscript a refers to the analyzed/optimized estimate after data assimilation, and F_{fix} represents the flux component that is not optimized in the inversion.

https://doi.org/10.5194/egusphere-2026-3879
Preprint. Discussion started: 27 July 2026

In addition to the flux scaling factors, the state vector also includes eight background parameters. These parameters are optimized together with the flux parameters in the EnKF update. They represent additive offsets of the initial and boundary conditions. Near the lateral boundaries, each grid cell is mainly controlled by its corresponding boundary-sector parameter, while farther inside the domain the correction is gradually blended toward the mean of all eight parameters to ensure a smooth transition.

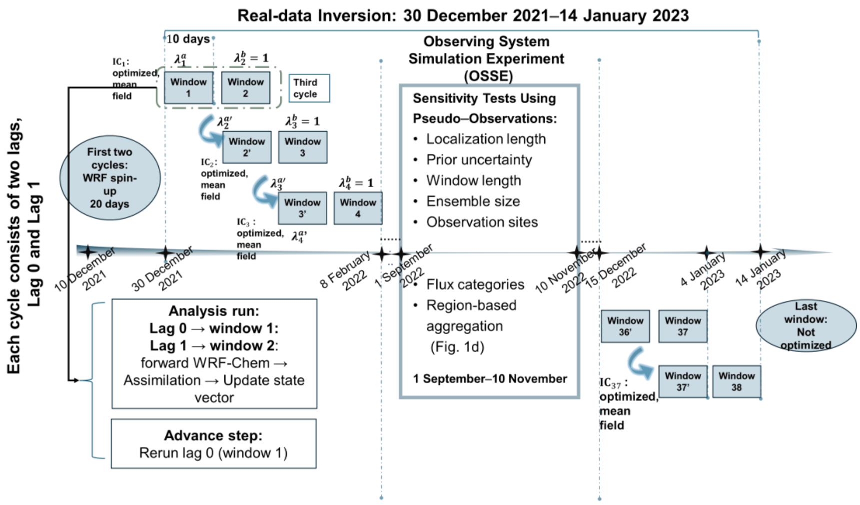

Figure 2: Workflow of CTDAS-WRF inversion for one year (30 December 2021–14 January 2023) and sensitivity tests for two months (1 September–10 November 2022). Here, IC_{k-2} denotes the initial concentration (IC) for the k-th cycle (excluding the two spin-up cycles).

2.2.2 Default inversion parameter setting

Following the comprehensive overview in Steiner et al. (2024), we provide specific descriptions of the CTDAS parameters that apply to this study. We adopt the setup of Steiner et al. (2024) and Ioannidis et al. (2026) given the comparable domain size, using 10-day flux windows with a fixed lag of 2. Consequently, observations within the twenty-day period constrain flux estimates for both the current window and the preceding window. For the ensemble size, we use 100 members for all experiments. The total number of state vector elements is 28574 in the default setup (six flux categories). The state vector size (N_{sv_tot}) follows Eq. (2):

$$N_{sv\_tot} = N_{proc} * N_{tiles} + N_{bg}, \tag{2}$$

where N_{proc} is the number of flux categories, N_{tiles} is the number of tiles and N_{bg} accounts for the number of initial and boundary parameters (8 by default). As shown in Fig. 1c, the "tile *r*" refers to the smallest spatial unit represented by one state vector element. One tile covers 54 km × 54 km, resulting in 4761 tiles.

Prior flux uncertainties are specified per grid cell as 30–40% for anthropogenic emissions and 50% for natural emissions as shown in Table 1, following earlier work (Qu et al., 2022; Saunois et al., 2025; Wang et al., 2025). To represent spatial error correlation during optimization, grid cells within the same emission category are correlated within a 300 km radius (exponential decay), while no cross-category correlation is assumed. We jointly optimize eight background mole-fraction parameters. This reduces the risk of misattributing background biases to local emission sources. To avoid an over-flexible background that could "absorb" emission signals, the prior uncertainty for each background parameter is constrained to 2 ppb (~1.0%) for the eight inflow regions where CH_4 from the CAMS global product enters the domain, as supported by the sensitivity analysis in Steiner et al. (2024) and applied by Ioannidis et al. (2026) for CTDAS-WRF.

The **R** matrix is diagonal and consists of reported measurement uncertainties and model-data mismatch (MDM) estimates, combined assuming they are independent. All stations are described in detail in Sect. 2.4. With reference to Tsuruta et al. (2017a), fixed and site-specific MDM values are assigned: 15 ppb for coastal and island stations sampling both land and ocean signals (HAT, YON, COI, ULD) and for the mountainous site with pronounced orography (RYO); 25 ppb for a predominantly land-influenced site (GSN); 40–50 ppb for stations with strong local variability (AMY, SORPES); and 50–100 ppb for stations showing very large mismatches with the forward simulation (SARI). For SARI, observations from 9 April to 31 December 2022 are assimilated, with the MDM set to 50 ppb from 9 April to 27 June and from 28 July to 5 September, and to 100 ppb from 28 June to 27 July and from 6 September to 31 December. These default MDM values are assigned according to site characteristics, including marine versus land influence, local variability, and the magnitude of persistent model-observation mismatches in short forward simulations.

To mitigate spurious long-range correlations in the EnKF, we apply covariance localization by multiplying the Kalman gain by a Gaussian distance-dependent tapering function (Peters et al., 2005):

$$\rho(d) = exp[-(\frac{d}{L})^2], \quad (3)$$

where d is the distance between the state element and the observation, and L is the localization length. In

https://doi.org/10.5194/egusphere-2026-3879
Preprint. Discussion started: 27 July 2026

this study, a default value of L = 900 km is used. This choice represents a compromise between suppressing spurious long-range updates and retaining sensitivity to regionally coherent observational signals. The localization length corresponds to roughly three times the flux correlation length (the exact multiple, obtained by comparing the integrals of the Gaussian localization function and the exponential correlation function, is $\frac{900km}{300km} * \frac{\sqrt{\pi}}{2} \approx 2.7$).

2.3 Experimental design

2.3.1 Observing System Simulation Experiment (OSSE)

An OSSE is designed to evaluate the performance of an inversion system in a fully controlled framework. In this study, WRF-Chem is driven and nudged to the analyzed meteorological fields together with a designated set of "true" fluxes (referred to as true state hereafter) to simulate a time series of CH_4 concentration fields. These simulated concentrations are then sampled at the same hour-specific times and locations as the real stations to generate pseudo-observations (Brasseur and Jacob, 2017). By comparing the inversion results constrained by these pseudo-observations with the prescribed true state, the OSSE framework allows us to assess the ability of the observing system to recover the true emissions (Sect. 3.1.1 and Sect. 3.1.2). Within this framework, the pseudo-observations are further used in a series of sensitivity tests, in which key inversion settings are systematically varied (Sect. 3.1.3). The same MDM settings as in the real-data inversion are used in the OSSE.

In this study, the prescribed true state is defined as twice the prior. Our sensitivity tests follow the approach of Steiner et al. (2024), which uses the same inversion system with a different atmospheric CTM (ICON-ART). As summarized in Fig. 2 and Table 2, the sensitivity tests assess the impact of key configuration choices. Hereafter, each sensitivity experiment is referred to as a "Case". Case 1 is the reference case, using the default settings described in Sect. 2.2.2. Cases 2–5 modify the ensemble size (150 members), window length (5 days), prescribed prior uncertainties (40% for all anthropogenic fluxes and 60% for natural fluxes), and localization length (600 km), respectively. Case 6 applies a region-based aggregation scheme (Fig. 1d). In Case 7, the flux categories are reduced to four by aggregating $E_{CH4\_proc\_5}$ (livestock sector) *and* $E_{CH4\_proc\_6}$ (the "Other" sector) into $E_{CH4\_proc\_3}$ (waste sector). In Case 8, SARI is included as an additional site. To specifically examine the effect of station coverage over the YRD in the default configuration, the other cases assimilate observations from eight stations (excluding SARI). Across all sensitivity tests, we perturb only the target parameter(s) of interest and keep

https://doi.org/10.5194/egusphere-2026-3879
Preprint. Discussion started: 27 July 2026

all remaining settings identical to the reference configuration.

For the region-based aggregation of the state vector (Case 6, Fig. 1d), we define tiles on a 9 km × 9 km grid obtained by subdividing D01 to the D02 resolution (Sect. 2.2.2). Land and ocean are separated using an external land-sea mask derived from the GEBCO_2024 Grid, a global 15 arc-second terrain model for ocean and land (GEBCO Bathymetric Compilation Group, 2024). Over land, tiles follow administrative boundaries, using cities within China and province-level administrative units elsewhere. Over the ocean, tiles follow a regular 1° × 1° latitude–longitude grid. Tiles smaller than 20 grid cells (9 km × 9 km) are merged into the dominant neighboring tile, and any remaining gaps are filled using the nearest valid tile. The resulting aggregation contains 1,359 tiles.

The OSSEs are conducted for the period from 1 September to 10 November 2022, which is chosen for computational feasibility. To reduce the influence of transport-model and initial-condition spin-up, we exclude the first two assimilation windows (1–20 September) from the final analysis. We also exclude the last assimilation window (31 October–10 November), because it is not followed by the same number of subsequent lagged windows as the earlier analysis periods.

2.3.2 Real-data inversion

This one-year inversion with CTDAS-WRF simulates the period from 10 December 2021 to 14 January 2023 and is constrained by real in situ observations. The first two cycles are used for WRF spin-up and are excluded from analysis, and the final window is not optimized by CTDAS-WRF. The effective results therefore span cycles 3–39 (30 December 2021–14 January 2023). From this period, we extracted results for the analyses from 1 January to 31 December, 2022.

2.4 Observation

A total of 12 ground-based observation sites are used in this study (Table 3). Seven of them, including AMY, COI, GSN, HAT, RYO, ULD and YON, are provided under the World Meteorological Organization’s Global Atmosphere Watch (GAW) program and archived by the World Data Centre for Greenhouse Gases (WDCGG). In addition, the Station for Observing Regional Processes of the Earth System (SORPES) is located on the Xianlin campus of Nanjing University (Ding et al., 2013). The SARI station of the Shanghai Advanced Research Institute, Chinese Academy of Sciences, is located on the rooftop of Building 1 on the Institute's campus (Wei et al., 2020). Data from both experimental sites are calibrated by the respective institutions. The SORPES station has been used in previous studies to assess

https://doi.org/10.5194/egusphere-2026-3879
Preprint. Discussion started: 27 July 2026

anthropogenic influences over rapidly urbanized and industrialized eastern China and to characterize the spatial and temporal variability of greenhouse gases in the YRD region (Ding et al., 2016; Zhao et al., 2024). The SARI station is situated in a densely developed scientific innovation and educational district and is therefore well positioned to capture the elevated CH_4 levels characteristic of the Shanghai megacity, providing complementary constraints for the inversion.

Furthermore, several additional sites in the YRD are used for independent evaluation, including the DMS station, a mountainous background site located in Damingshan, Zhejiang. Total column measurements have been used from the HF and SH stations. The HF station is located in Hefei, and its data are obtained from the Total Carbon Column Observing Network (TCCON), a global network of ground-based high-resolution Fourier transform spectrometers that record direct solar spectra in the near-infrared spectral region. The SH station is located in Shanghai, and the data are provided by the Shanghai Advanced Research Institute, Chinese Academy of Sciences at the same site as SARI. The locations of all three sites are shown in Fig. S1. For the comparison with total-column measurements, the missing CH_4 concentrations between the upper boundary of the WRF-Chem profiles and 50 hPa are supplemented with background profiles from the CAMS global inversion-optimized greenhouse-gas flux reanalysis (Sect. 2.1.2). For SH, where site-specific auxiliary data (e.g., averaging kernels and prior profiles) are unavailable, model XCH_4 is calculated as a pressure-weighted dry-air column average. For HF, the model profile is converted to a TCCON-equivalent dry-air XCH_4 by applying the TCCON averaging kernel (Laughner et al., 2024; Tsuruta et al., 2023):

$$x_{model,wet,i} = x_{model,dry,i}\,(1 - q_{H2O}), \tag{4}$$

$$\mathrm{XCH}_{4,ak} = \mathrm{X}_a + \sum_i \omega_i\, a_i\,(x_{model,wet,i} - x_{a,wet,i}), \tag{5}$$

where $x_{model,wet,i}$ and $x_{model,dry,i}$ are the model (WRF-Chem) CH_4 wet and dry mole fractions at vertical layer i, q_{H2O} is the wet mole fraction of water vapor retrieved by TCCON, X_a is the TCCON prior dry-air XCH_4, ω_i is the TCCON column integration operator, a_i is the XCH_4 averaging kernel, and $x_{a,wet.i}$ are the TCCON prior CH_4 wet mole fractions at layer i. The resulting AK-smoothed model-equivalent XCH_4 is compared with the observed TCCON dry-air XCH_4.

For non-mountain sites, we retain only observations between 09:00 and 16:00 local time to sidestep the challenges posed by shallow nocturnal boundary layers. For the mountain site, we retain observations

https://doi.org/10.5194/egusphere-2026-3879
Preprint. Discussion started: 27 July 2026

between 23:00 and 06:00 local time because these hours better reflect free-tropospheric conditions and minimize the influence of daytime upslope valley winds. As a result, the selected mountain observations are expected to have representativeness errors comparable to those at coastal background sites, and the same model-data mismatch (15 ppb) is therefore adopted. We further control for representativeness using a wind-based filter, following Zhang et al. (2022). CH_4 measurements are excluded when surface winds indicate influence from nearby sources (e.g., villages, factories, or paddy rice fields). To reduce local source and sink effects, measurements are also excluded when wind speed is below 1.5 m s^{-1} or above 10 m s^{-1}, since higher speeds can transport emissions from a broader area. The remaining data are considered regionally representative and used in the analysis.

https://doi.org/10.5194/egusphere-2026-3879
Preprint. Discussion started: 27 July 2026

Table 2: Overview of the synthetic simulations. Boldface numbers or text signify changes.

Case	Localization length (km)	Prior uncertainty		Sites	Window length (days)	Region-based aggregation	Flux category	Members	Note
		Anthropogenic	Natural						
1	900	0.3-0.4	0.5	8	10	No	6	100	Reference
2	900	0.3-0.4	0.5	8	10	No	6	**150**	Sensitivity tests
3	900	0.3-0.4	0.5	8	**5**	No	6	100	
4	900	**0.4**	**0.6**	8	10	No	6	100	
5	**600**	0.3-0.4	0.5	8	10	No	6	100	
6	900	0.3-0.4	0.5	8	10	**Yes**	6	100	
7	900	0.3-0.4	0.5	8	10	No	**4**	100	
8	900	0.3-0.4	0.5	**9**	10	No	6	100	

https://doi.org/10.5194/egusphere-2026-3879
Preprint. Discussion started: 27 July 2026

Table 3: The observation sites used in this study. Site types are defined based on geographic location.

Site ID	Location	Reference	Longitude (° E)	Latitude (° N)	Elevation (m)	Sample altitude (m)	Site type	MDM (ppb)	Purpose	Notes
HAT	Hateruma Island	Tohjima (2025b)	123.81	24.06	10	47	Island	15	Inversion	2022
YON	Yonagunijima	Takatsuji (2024b)	123.01	24.47	30	50	Island	15		2022
SARI	Shanghai	Wei et al. (2020)	121.59	31.18	--	~20	Urban	50, 100		9 April–31 December
SORPES	Nanjing	Ding et al. (2016)	118.95	32.12	40	112	Urban	50		1 February–16 April, 7 July–13 November
GSN	Gosan	Yang (2024b)	126.16	33.29	71.4	77.4	Island	25		2022
AMY	Anmyeon-do	Yang (2024a)	126.33	36.54	42	108	Coastal	40		2022
ULD	Ulleungdo	Yang (2024c)	130.90	37.48	220.9	230.9	Island	15		2022
RYO	Ryori	Takatsuji (2024a)	141.82	39.03	260	280	Mountain	15		2022
COI	Cape Ochiishi	Tohjima (2025a)	145.50	43.16	42.4	93.9	Coastal	15		2022
DMS	Damingshan		119.00	30.02	1497	1512	Mountain		Validation	2022
SH	Shanghai		121.59	31.18						2022
HF	Hefei (TCCON)	Liu et al. (2023)	117.17	31.91						2022

https://doi.org/10.5194/egusphere-2026-3879
Preprint. Discussion started: 27 July 2026

3 Results and discussion

3.1 Observing System Simulation Experiment (OSSE): spatial scope of flux constraint and sensitivity tests

Based on eight inversion cases (1 September–10 November 2022), even under limited observational coverage, our inversion is still able to effectively constrain CH_4 fluxes in observation-rich regions over East Asia, including the Yangtze River Delta (YRD), South Korea, and northern Japan (north of 37°N) (Sect. 3.1.1), and to significantly reduce uncertainties in emissions from major sectors (Sect. 3.1.2). We also identify several key parameters that influence inversion performance (Sect. 3.1.3). Together, these findings provide a solid basis for the subsequent analysis of the YRD (Sect. 3.2).

3.1.1 Flux recovery and concentration field assessment

Figure 3 shows the comparison of posterior and prior emission for the OSSE in which the true state is prescribed as twice the prior. Positive adjustments dominate over Japan, South Korea, and central China, indicating markedly higher posterior than prior emissions (Fig 3a). The largest signals occur in observation-rich regions (the YRD, South Korea, and northern Japan) and also over a localized coal-mine hotspot in Shanxi Province (34.57–40.73°N, 110.23–114.55°E), where strong emissions generate pronounced gradients. In the surrounding land areas of the observation-rich areas (e.g., the provinces around the YRD and parts of North Korea), adjustments are weaker, whereas changes are near zero elsewhere. Over the ocean, differences are negligible because ocean fluxes are not optimized and their magnitudes are small; consequently, they do not noticeably contribute to the difference map.

Negative adjustments are limited but detectable, occurring mainly over northern Taiwan and nearby islands. Although these signals are co-located with the island stations HAT and YON, their spatial extent and magnitude are much smaller than those over the three main observation-influenced regions discussed below. In addition, small patchy adjustments of both signs appear over parts of Russia and northeast China. These remote signals most likely result from residual spurious long-range correlations introduced by the finite ensemble size, which localization reduces but does not completely remove (Houtekamer and Mitchell, 1998; Steiner et al., 2024). The posterior-to-prior ratio supports the same conclusion (Fig. 3b). Ideally, posterior fluxes would be close to twice the prior. In our setup, however, coherent large-scale scaling is mainly restricted to three observation-influenced regions: South Korea, northern Japan (north of 37°N), and the YRD. Among these, the clearest adjustment is found over northern Japan. Outside these

https://doi.org/10.5194/egusphere-2026-3879
Preprint. Discussion started: 27 July 2026

regions, the inferred scaling decays rapidly and becomes negligible with increasing distance.

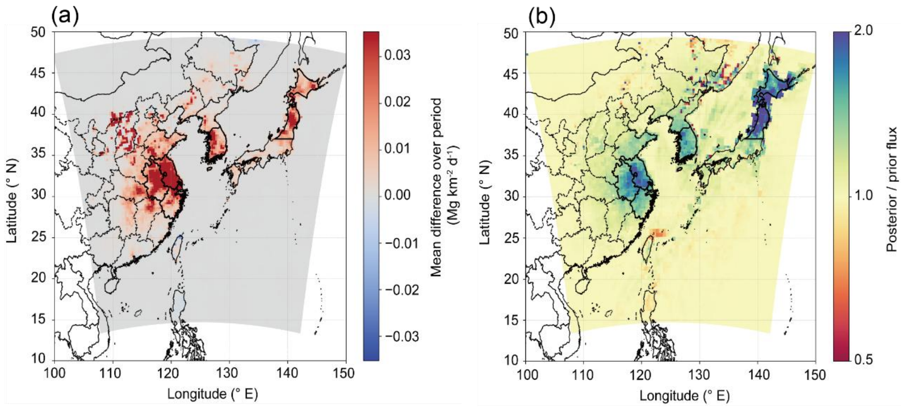

Figure 3: Map showing the time-averaged (21 September–30 October 2022) CH_4 emission (a) difference between posterior and prior (posterior minus prior, in Mg km^{-2} d^{-1}) and (b) posterior-to-prior ratio over the parent domain (D01). Values of the posterior-to-prior ratio greater than 2.0 (0.6% grids) are shown in the same color as 2.0.

Among the three selected observation-rich regions, the YRD is the largest contributor, accounting for 12.1% of the prior parent domain total (Fig. 4a–d). Emissions over South Korea and northern Japan (north of 37°N) are much smaller (2.1% and 1.6%, respectively), with prior hourly emissions ranging from 114 to 171 Mg h^{-1}. Taiwan is not included in this regional analysis. Because despite the presence of nearby island stations, the inferred flux adjustments and concentration responses there are much weaker and less spatially coherent than in the three focus regions, indicating substantially weaker observational constraint.

At the scale of the whole parent domain, the inversion produces only a modest net change, with the domain-total posterior about 22.5% higher than the prior. Regionally, however, much larger changes are observed: across the three focus areas, the posterior departs from the prior by 60.8% in the YRD, 67.9% in South Korea, and 92.7% in northern Japan, bringing the estimates substantially closer to the prescribed true state. Northern Japan shows the best agreement after optimization; from 21 September to 1 October, the posterior and true-state curves nearly overlap for much of the period. For South Korea, the posterior varies noticeably across assimilation windows, with the 10-day correction rate [defined as (posterior-prior)/prior × 100%] ranging from 36.6% to 86.2%. The YRD posterior likewise moves toward the true-state emissions, but the adjustments are more muted in some subregions, for example, over the

https://doi.org/10.5194/egusphere-2026-3879
Preprint. Discussion started: 27 July 2026

northwestern YRD, where the very high fuel-exploitation emissions remain only partly corrected. This likely reflects weaker local observational constraint due to the limited observational coverage relative to the spatial extent of the region.

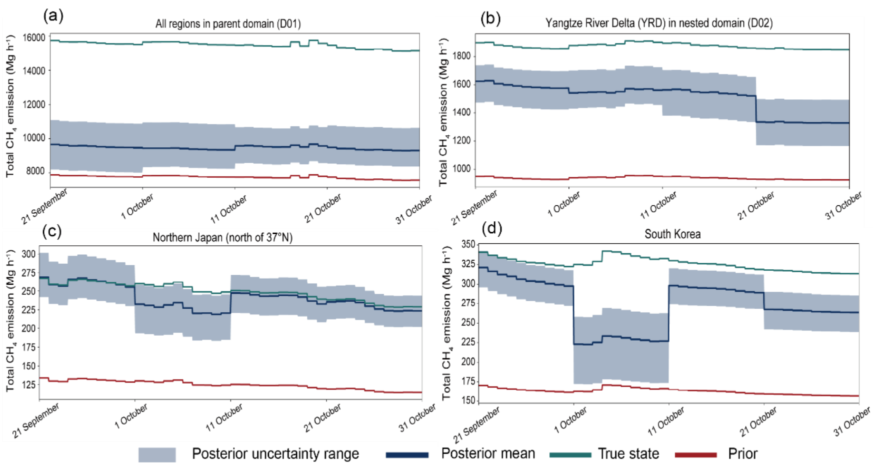

Figure 4: Temporal variation of hourly CH_4 emissions (21 September–30 October 2022, in Mg h^{-1}) for the prior, posterior, and true-state emissions over (a) the parent domain (D01), (b) the YRD, (c) northern Japan (north of 37°N), and (d) South Korea.

A comparison of the time-averaged near-surface CH_4 concentration fields (21 September–30 October 2022) simulated with different emissions shows that the posterior and true-state cases exhibit nearly identical large-scale patterns, with enhanced concentrations over central China and the northern YRD (Fig. S2a–c). The main difference is that the posterior case partially recovers the peak concentrations, but still fails to reproduce most of the high-concentration regions seen in the true-state case. In particular, over parts of central and western China between 30°N and 40°N, as well as in southern China, including the Pearl River Delta, the time-averaged concentrations remain close to those in the prior case, consistent with the prior-minus-posterior difference field (Fig. 5c). Compared with the prior-minus-true-state differences shown in Fig. 5d, the posterior-minus-true-state differences in Fig. 5e are markedly reduced. The discrepancies are largely removed over the central YRD, although notable differences remain in the northwestern part of the domain. This area is mainly affected by strong local fuel exploitation emissions, for which the posterior adjustment remains limited, likely owing to the larger distance from the observation sites (Sect. 3.1.2). Over the YRD, the mean concentration mismatch relative to the true-state field decreases from about 318 ppb in the prior case to about 129 ppb in the posterior case, corresponding

https://doi.org/10.5194/egusphere-2026-3879
Preprint. Discussion started: 27 July 2026

to a reduction of about 59.5%. Similar improvements are found in the other two observation-rich regions. Over South Korea, the mean mismatch decreases from about 175 to 57 ppb, a reduction of about 67.5%, while over northern Japan it decreases from about 78 to 16 ppb, corresponding to a reduction of about 79.5%.

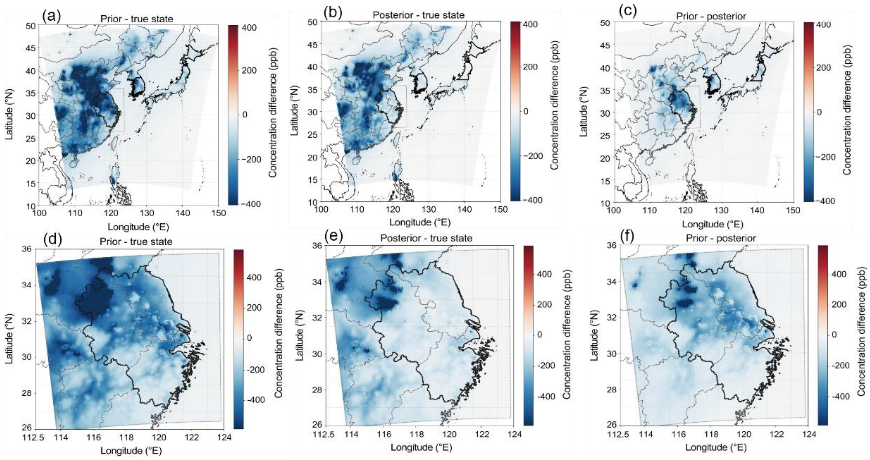

Figure 5: Time-averaged (21 September–30 October 2022) near-surface CH_4 concentration fields differences for (a, d) prior minus true state, (b, e) posterior minus true state, and (c, f) prior minus posterior, shown over the full parent domain (a–c) and the nested domain (d–f).

3.1.2 Sector-specific constraint performance within the YRD

The total posterior-to-prior emission ratios indicate that most areas are adjusted by the inversion (Fig. 6a), whereas the southern and northwestern parts of the YRD show much weaker update. The only local observation site (SORPES station) is too distant for these areas, such that their separation far exceeds the prescribed correlation length and the corresponding flux-concentration correlation becomes very weak (van der Laan-Luijkx et al., 2017), leading to the darkest-colored regions (posterior closest to the true state) being concentrated mainly in the northeastern YRD. Based on the spatial patterns of the posterior-to-prior ratios by sector, the inversion performs best for the rice cultivation, natural and waste sectors, for which the posterior maps most closely reproduce the prescribed true state (Fig. 6b-d). Fuel-exploitation adjustments are weaker and mainly confined to the northern high-emission areas (Fig. 6e–f). The "Other" and livestock sectors account for only a small fraction of the regional total (~3.5–5.6%; Fig. 6h), and their adjustments are less stable, likely because their smaller prior fluxes produce weaker atmospheric signals and are more susceptible to spurious correlations.

https://doi.org/10.5194/egusphere-2026-3879
Preprint. Discussion started: 27 July 2026

Consistent with the spatial patterns discussed above, the frequency distribution of grid-cell posterior-to-prior ratios highlights clear sectoral differences in the inversion response (Fig. 6i). The natural sector shows the strongest adjustment toward the prescribed true state, with a YRD-integrated posterior-to-prior emission ratio of 2.2. At the grid-cell level, 40.6% of valid cells fall within the 1.8–2.2 range and another 29.4% exceed 2.2, indicating strong upward corrections over much of the YRD. Rice cultivation sector also shows a clear positive adjustment, with a YRD-integrated ratio of 1.6; most grid cells are concentrated in the 1.4–1.8 range (77.0%), while only 3.7% reach 1.8–2.2. Waste sector exhibits a similar but slightly weaker response, with a YRD-integrated ratio of 1.5 and 64.4% of grid cells within 1.4–1.8. Fuel exploitation sector shows more moderate corrections, with a YRD-integrated ratio of 1.4; most cells fall within 1.0–1.4 (71.8 %), although 27.2 % still reach 1.4–1.8. By contrast, the livestock and "Other" sectors show the weakest and least spatially consistent responses, with YRD-integrated ratios of 1.1 and 1.0, respectively. For these two sectors, 22.4% and 38.7% of grid cells are below 1.0, while the remaining cells mostly lie within 1.0–1.4. Overall, these sectoral histograms and maps confirm substantial differences in inversion performance across flux categories. Nevertheless, under the current observational configuration, the inversion still provides strong constraints and clear optimization signals in the vicinity of the observing site.

https://doi.org/10.5194/egusphere-2026-3879
Preprint. Discussion started: 27 July 2026

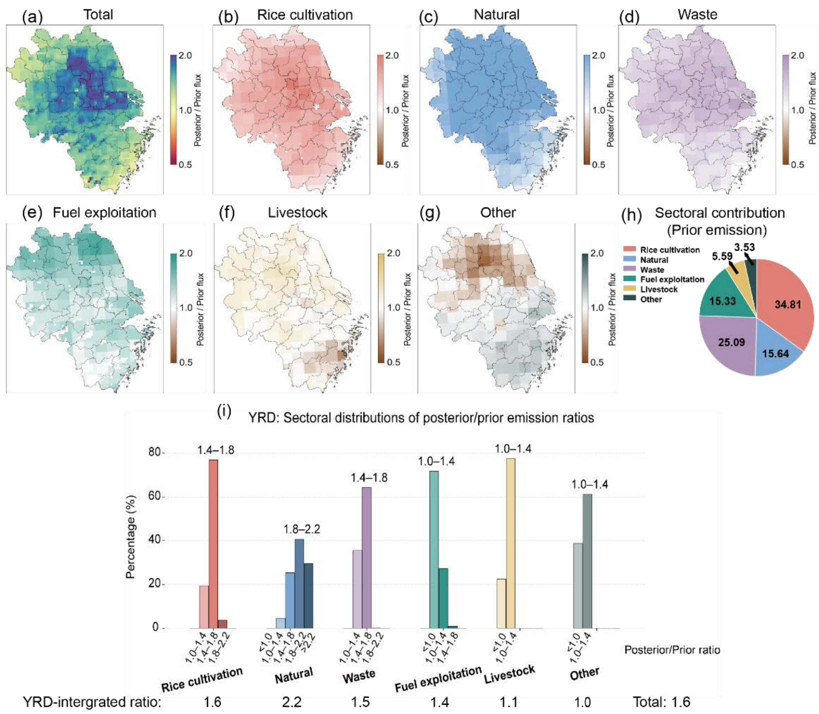

Figure 6: Spatial distribution of the posterior-to-prior emission ratio over the YRD for (a) total emissions and the (b) rice cultivation, (c) natural, (d) waste, (e) fuel exploitation, (f) livestock, and (g) "Other" sectors; (h) pie chart of the prior sectoral emission fractions; and (i) sectoral frequency histograms of the posterior-to-prior ratios across YRD grid cells.

3.1.3 Sensitivity of inversion performance to parameter settings

Table 4 summarizes the error reduction in total and sectoral emissions for the sensitivity tests over two regions (the parent domain and the YRD). Here, C_{mae} denotes the percentage reduction in mean absolute error (MAE) from the prior to the posterior relative to the true state, where M^e_{prior} and M^e_{post} are the MAEs of the prior and posterior fluxes against the grid-cell true-state fluxes within a given region. The metric is computed at each time step and then averaged over the full analysis period.

For the reference case, C_{mae} over the full parent domain (D01) ranges from 3.0% to 25.0% across individual sectors and the total flux. In the YRD, error reduction is consistently larger, with the total-flux MAE reduced by 55.7% after inversion. The strongest YRD error reduction is found for rice cultivation (57.7%), followed by natural emissions (49.8%) and waste (48.9%). Fuel exploitation also shows a moderate improvement (39.8%), whereas the smaller-contribution livestock and "Other" sectors show much weaker improvements, with C_{mae} values of 13.7% and 4.5%, respectively.

https://doi.org/10.5194/egusphere-2026-3879
Preprint. Discussion started: 27 July 2026

For the total flux over D01, parameter changes that yield a positive impact on flux error reduction include increasing the ensemble size from 100 to 150 members (Case 2), increasing the prior uncertainty (anthropogenic to 40 % and natural to 60 %; Case 4), using fewer flux categories (Case 7), and adding additional observing sites (Case 8). For the YRD, increasing the ensemble size (Case 2) produces the largest improvement in total flux C_{mae} (+6.5 percentage points), followed by reducing the number of flux variables (Case 7; +5.7 percentage points) and applying the region-based aggregation of the state vector (Case 6; +4.7 percentage points). The region-based aggregation improves the total-flux error reduction over the YRD but has little impact on the parent-domain total flux.

Two adjustments weaken the total-flux error reduction: decreasing the localization length from 900 to 600 km (Case 5) and shortening the assimilation window from 10 to 5 days (Case 3). For the total flux over D01, C_{mae} decreases by 7.1 percentage points in Case 5 and by 2.4 percentage points in Case 3, while the decreases over the YRD are smaller (3.4 and 0.8 percentage points, respectively). This indicates that the inversion is sensitive to the spatial and temporal extent of observational influence: shorter localization limits the propagation of information through the Kalman gain, whereas a shorter window weakens the connection between transported emission signals and the observing network.

When comparing our sensitivity results with those reported by Steiner et al. (2024), we find several consistent conclusions. First, increasing the ensemble size within a reasonable range leads to a clear improvement in inversion performance. Second, the localization length plays a central role because it directly shapes the Kalman gain; reducing the localization length from about three to roughly two times the correlation length substantially weakens the error reduction. In addition, using fewer flux categories effectively reduces the size of the state vector and can improve error reduction for the aggregated sectors. After merging the livestock and "Other" sectors into the waste sector, C_{mae} for waste increases from 20.7% to 22.4% over D01 and from 48.9% to 60.9% over the YRD. Adding additional observing sites also improves the total-flux error reduction over both D01 and the YRD.

The region-based aggregation has a positive effect on the total YRD flux and dominant sectoral fluxes. The C_{mae} increases markedly for fuel exploitation (+18.6 percentage points) and rice cultivation (+8.6 percentage points). However, it reduces the error reduction for natural emissions from 49.8% to 37.9%, and leads to negative or near-zero performance for the livestock and "Other" sectors in the YRD. The poorer natural-sector performance likely arises because administrative aggregation imposes one scaling

https://doi.org/10.5194/egusphere-2026-3879
Preprint. Discussion started: 27 July 2026

factor over areas where natural fluxes remain spatially heterogeneous and are mainly controlled by environmental conditions. It stabilizes dominant anthropogenic sectors, but livestock and "Other" remain poorly constrained because their small fluxes generate weak signals that are more sensitive to sampling noise and cross-sector compensation. Thus, the aggregation improves total and dominant-sector estimates, but weakens attribution for heterogeneous or weakly constrained sectors.

Adding a site in Shanghai improves total-flux C_{mae} to 21.6% over D01 and 58.8% over the YRD. Within the YRD, the largest gains are found for rice cultivation and waste, for which C_{mae} reaches 63.0% and 60.3%, respectively. Increasing the prior uncertainty has an effect similar to reducing the model-data mismatch in Steiner et al. (2024), as both changes shift the inversion toward stronger reliance on the observations rather than on the prior inventory. In our Case 4, the increased prior uncertainty improves total-flux C_{mae} over both D01 and the YRD (59.5%) and enhances the error reduction for most major sectors, although the response is not uniform across all source categories.

https://doi.org/10.5194/egusphere-2026-3879
Preprint. Discussion started: 27 July 2026

Table 4: Statistical summary of the sensitivity tests for the analysis period (21 September–30 October 2022). The C_{mae} quantifies the reduction in mean absolute error of the posterior fluxes relative to the prior, evaluated against the true-state fluxes. Statistics are computed for total and sectoral emissions over the parent domain (D01) and the YRD, computing at each time step and then averaged over the full analysis period.

Case	Sensitivity	$C_{mae} = 1 - \frac{M^e_{post}}{M^e_{prior}}$ (%)													
		Total flux		Rice cultivation		Natural		Waste		Fuel exploitation		Livestock		Other	
		D01	YRD	D01	YRD	D01	YRD	D01	YRD	D01	YRD	D01	YRD	D01	YRD
1	Reference	20.8	55.7	21.3	57.7	25.0	49.8	20.7	48.9	18.8	39.8	7.5	13.7	3.0	4.5
2	Members	21.3	62.2	20.9	64.6	25.6	39.1	20.8	61.3	22.1	67.7	6.1	8.5	5.7	14.5
3	Window length	18.4	54.9	21.4	57.7	22.8	51.1	18.1	44.1	13.4	33.6	8.1	8.4	5.7	10.8
4	Prior uncertainty	21.8	59.5	23.9	61.0	25.8	51.6	24.5	58.3	16.9	37.8	9.4	20.2	4.0	4.9
5	Localization length	13.7	52.3	15.6	51.3	22.0	57.0	15.1	46.8	6.7	34.5	6.5	14.1	3.1	9.1
6	Region-based aggregation	20.7	60.4	20.8	66.3	23.5	37.9	20.3	50.4	19.9	58.4	3.9	-9.6	3.5	-1.0
7	Flux category	21.1	61.4	18.5	61.4	22.7	35.8	22.4	60.9	14.6	28.9				
8	Sites	21.6	58.8	23.0	63.0	25.0	45.1	22.7	60.3	18.8	31.3	7.0	12.5	2.8	1.4

https://doi.org/10.5194/egusphere-2026-3879
Preprint. Discussion started: 27 July 2026

3.2 Real-data inversion in 2022: posterior emission estimates, uncertainty reduction, and inversion diagnostics

The real-data inversion shows that existing bottom-up inventories are generally biased high and display substantial spatial discrepancies of posterior CH_4 emission (Sect. 3.2.1). In the YRD, the prior emissions underestimate the summer peak and overestimate emissions during the rest of the year, with the seasonal correction driven mainly by rice cultivation and natural emissions (Sect. 3.2.2). The inversion remains less effective at constraining weaker sources. However, uncertainty reduction is substantial in the main source regions, and posterior inter-sector coupling over the YRD remains weak overall, despite residual trade-offs among some sector pairs (Sect. 3.2.3).

3.2.1 Annual total and sectoral posterior emissions and optimized lateral boundary conditions

We find that the major emission hotspots are concentrated in central and eastern China, as well as the Pearl River Delta in southern China (Fig. 7a–b). The prior emissions are substantially higher than the posterior estimates over the YRD region, Shanxi, and northern Japan (north of 37°N), whereas underestimation is mainly found over western South Korea and the eastern part of Hubei province in China (29.97–31.37°N, 113.68–115°E) (Fig. 7c). More specifically, within the YRD region, emissions are mainly concentrated in northern Anhui, southern Jiangsu, and Shanghai (Fig. 7d–e). These same areas also exhibit the most pronounced prior overestimation in the posterior minus prior comparison (Fig. 7f). In contrast, a localized area in southwestern Anhui shows an underestimation, although its magnitude is relatively small (less than 10 Mg km^{-2} yr^{-1}).

Among the four provincial-level regions in the YRD, Anhui has the largest CH_4 emissions and is dominated by rice cultivation and fuel exploitation (Fig. 8a). The annual CH_4 emissions from fuel exploitation are overestimated by 0.22 Tg yr^{-1}, corresponding to a posterior reduction of 22.2%. In contrast to the other three regions, natural emissions in Anhui are underestimated by 12.9% (0.07 Tg yr^{-1}). Compared with Anhui, Jiangsu shows higher emissions and stronger decreases from the prior to the posterior in the rice cultivation, natural, and waste sectors, with the largest absolute waste adjustment (19.5%, 0.15 Tg yr^{-1}) among the four regions (Fig. 8b). Shanghai is dominated by waste and fuel exploitation, which are overestimated by 0.08 Tg yr^{-1} (33.1%) and 0.02 Tg yr^{-1} (17.9%), respectively (Fig. 8c). Zhejiang is dominated by rice cultivation and waste, with posterior reductions of 0.08 Tg yr^{-1} (9.4%) and 0.11 Tg yr^{-1} (21.1%), respectively (Fig. 8d).

https://doi.org/10.5194/egusphere-2026-3879
Preprint. Discussion started: 27 July 2026

Spatially, emissions of the rice cultivation sector are mainly located near the Yangtze River estuary, particularly in northern Zhejiang (Fig. S3a–b). Prior natural emissions are primarily underestimated in southwestern Anhui (Fig S4d–f), whereas the emissions are mainly overestimated in southern Jiangsu. Waste exhibits a more point-like pattern across the central and coastal YRD, with a particularly strong signal over Shanghai (Fig. S3g–i). Emissions from the fuel exploitation and livestock sectors are largely concentrated in northern Anhui, and they are consistently reduced after inversion (Fig. S3j–o). However, they may remain weakly constrained, as even the nearest stations in Nanjing and Shanghai are still too distant to produce substantial adjustments in the main emitting areas (Fig. 6). The "Other" sector shows only small adjustments, with prior underestimation over the central YRD and prior overestimation over the eastern YRD (Fig. S3p–r).

For the annual-mean spatial difference in the boundary background field (posterior minus prior; Fig. 9), the adjustment ranges from -0.7 to 0.2 ppb. Positive adjustments are mainly found along much of the northern boundary and the upper part of the eastern boundary, indicating prior underestimation there. By contrast, negative adjustments are pronounced over the southeastern oceanic sector and the northwestern inland sector, indicating prior overestimation in these regions; adjustments elsewhere are generally weak and close to zero. The boundary background corrections remain modest but exhibit a clear seasonal reversal. Positive adjustments peak in July to September, particularly along the northern and northeastern boundaries, whereas negative adjustments dominate in January to March and October to December (Fig. S4a-d). In general, the magnitude of the adjustments remains modest and broadly comparable to the background corrections reported by Steiner et al. (2024) for their European station inversions.

https://doi.org/10.5194/egusphere-2026-3879
Preprint. Discussion started: 27 July 2026

620 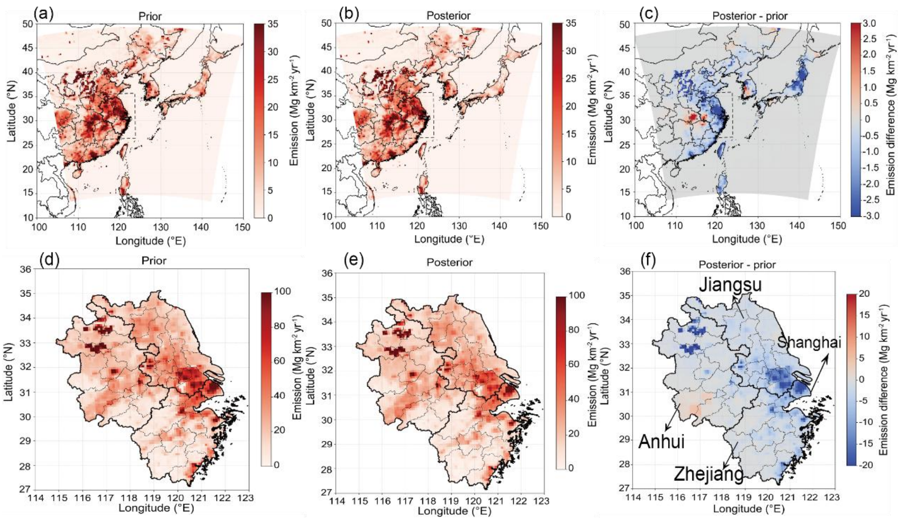

Figure 7: Annual-averaged CH_4 emissions (1 January–31 December 2022, in Mg km^{-2} yr^{-1}) for (a, d) prior, (b, e) posterior, and (c, f) difference (posterior minus prior) over the parent domain (a–c) and the YRD region (d–f).

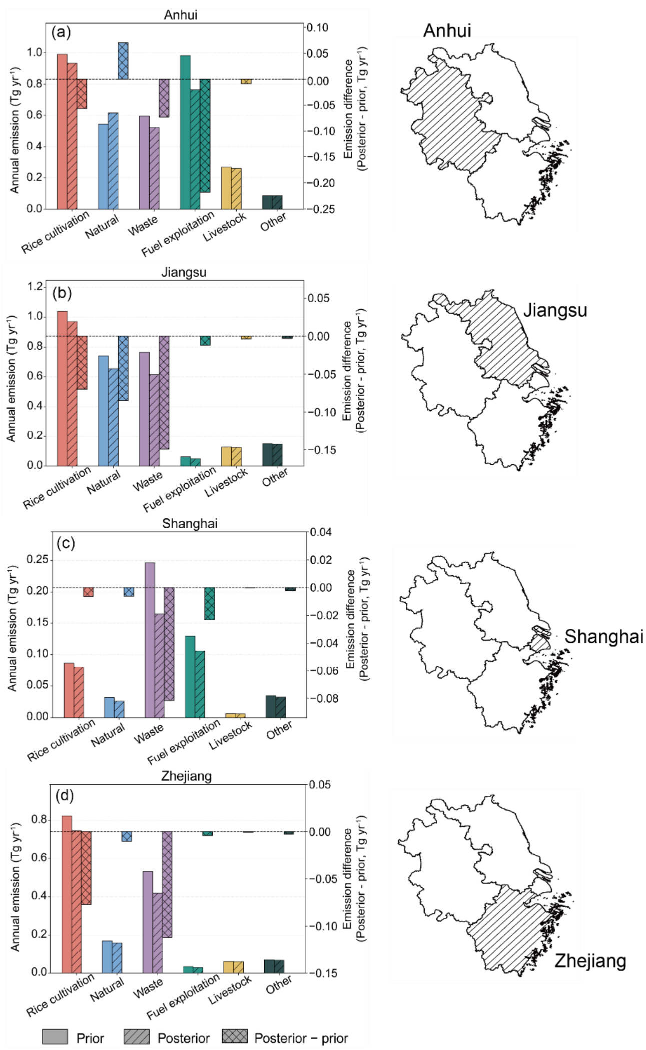

625 **Figure 8: Annual-averaged CH_4 emission (1 January–31 December 2022, in Tg yr^{-1}) and difference (posterior minus prior) across different sectors in (a) Anhui, (b) Jiangsu, (c) Shanghai, and (d) Zhejiang in the YRD.**

https://doi.org/10.5194/egusphere-2026-3879
Preprint. Discussion started: 27 July 2026

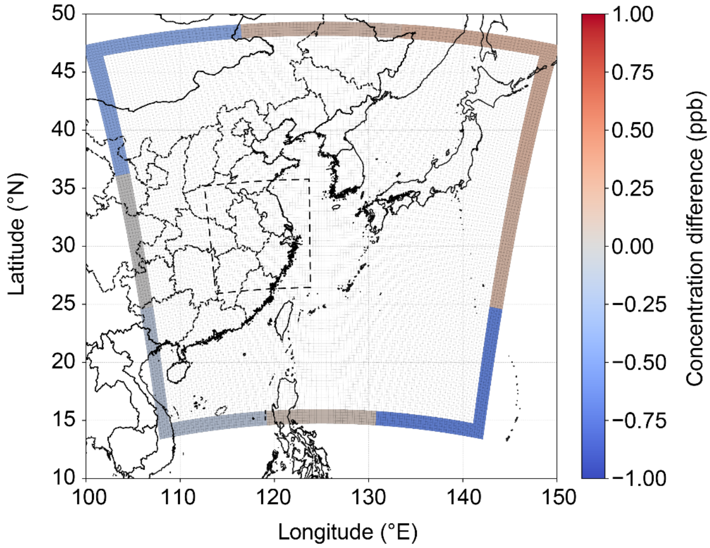

Figure 9: Annual-averaged difference (Posterior minus prior) in surface CH_4 boundary concentrations between the posterior and prior cases during 2022.

3.2.2 Seasonal variability and sectoral drivers of YRD CH_4 emissions

We summarize the temporal variability of total CH_4 emissions in the YRD region (Fig. 10a), together with the daily differences (posterior minus prior) and their sectoral contributions (Fig. 10b). Over the YRD, the prior emissions exhibit only weak seasonality, remaining nearly constant throughout the year within a narrow range of 0.022 to 0.025 Tg d^{-1}. By contrast, the posterior emissions show a clearer seasonal cycle, with deviations from the prior range from -52.1% to +61.0%. The posterior emissions reach a summer maximum of about 0.04 Tg d^{-1} in July to August, while its seasonal amplitude is about 0.03 Tg d^{-1}, roughly one order of magnitude larger than that of the prior (0.003 Tg d^{-1}). Posterior emissions are substantially higher than the prior from June to mid-September and lower during the remainder of the year.

The sectoral breakdown indicates that the adjustment is dominated by a few sectors. Rice cultivation contributes most of the prior overestimation (0.55 Tg, 31%; Fig. 10c), mainly concentrated in January–April, but becomes a major underestimation contributor during June to September (0.34, 40.4%; Fig. 10d). The posterior shows a broad summer enhancement in rice-cultivation emissions, whereas both the Global Rice Paddy Inventory (GRPI; Chen et al., 2025) and CAMS inversion-optimized fluxes (CAMS v25r1; Bergamaschi et al., 2013) indicate stronger summer peaks. GRPI exhibits the sharpest and most pronounced August maximum, while CAMS v25r1 shows a broader and more sustained enhancement from June to August. The posterior seasonal amplitude is weaker than both datasets (Fig. S5). Natural emissions also make a major contribution to the summertime prior underestimation (0.35 Tg, 41.7%) over the YRD. As shown in Fig. S3d–f, their annual underestimation is concentrated in southwestern Anhui. According to East et al. (2024) and Chen et al. (2013), this may partly reflect enhanced wetland CH_4 release during the warm season. Our result for the summertime contributions of these two sectors is broadly consistent with the 2018 estimate derived by Huang et al. (2021) from tower-based regional analysis, although the relative sectoral contributions differ.

The waste and fuel exploitation sectors are predominantly overestimated. The waste sector provides the second-largest contribution to the total overestimation, explaining 26.7% (0.47 Tg) over the YRD. Nevertheless, waste emissions remain underestimated in August, consistent with the findings of Hu et al. (2023) and Sun et al. (2026) that CH_4 emissions from wastewater systems increase under warmer conditions. The contribution of fuel exploitation emissions to the total overestimation is 17.8% (0.32 Tg) for the YRD. Adjustments in livestock and the "Other" sectors are negligible (less than 3.0%).

Overall, the optimized seasonal behavior is consistent with previous studies showing stronger summer emissions from rice cultivation and natural sources over eastern China. However, the CH_4 soil sink is prescribed as a fixed prior field rather than optimized, its seasonal variability is retained but not adjusted by the inversion, and the inferred summer maximum should therefore be interpreted under this fixed-sink assumption.

https://doi.org/10.5194/egusphere-2026-3879
Preprint. Discussion started: 27 July 2026

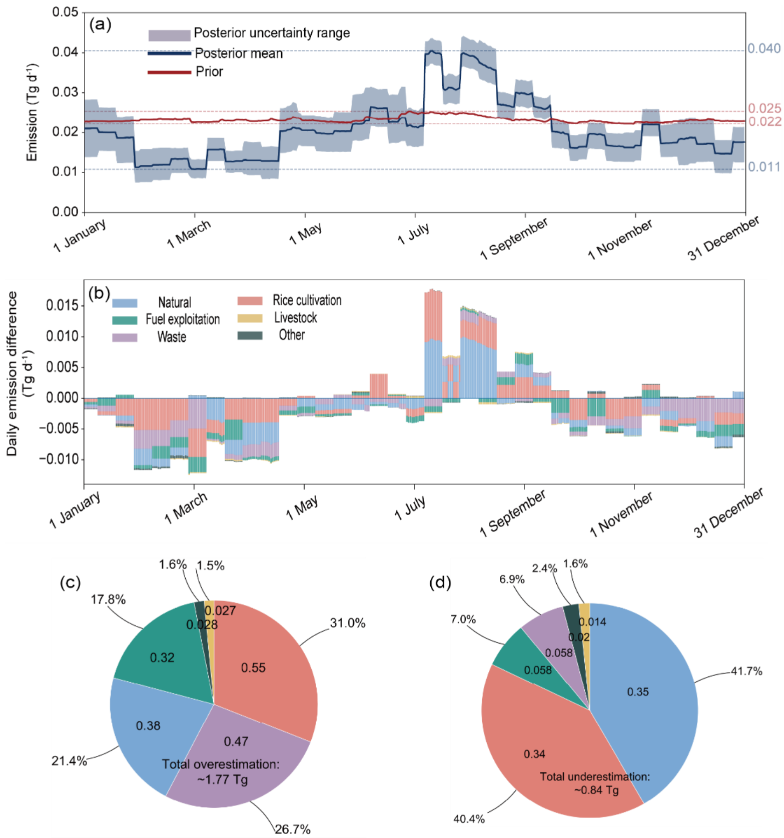

Figure 10: Temporal evolution of CH_4 emissions from the prior and posterior estimates, shown as (a) time series, and (b) the corresponding daily differences (posterior minus prior, in Tg d^{-1}) with sectoral contributions for the YRD region during 2022. Panels (c) and (d) show the sectoral contributions to the total prior overestimation and underestimation of CH_4 emissions (in Tg), respectively. In panel (b), sectors are arranged from the center outward, from largest to smallest. Prior underestimation is shown above the x axis, and prior overestimation below it.

3.2.3 Spatial patterns of posterior flux uncertainty reduction

Figure S6 summarizes the spatial distribution of total and sector-specific uncertainty reduction in CH_4 emissions. Here, uncertainty reduction is defined as the fractional decrease in ensemble spread, measured by the standard deviation across ensemble members from the prior to the posterior. Sector-specific reductions are calculated for each sectoral state vector and then mapped to the grid. Total uncertainty reduction is calculated from the ensemble spread of the total grid-cell flux. Across the parent domain, uncertainty reduction is clearly concentrated in three observation-influenced regions: the YRD region, South Korea, and northern Japan (north of 37°N) (Fig. S6a). Averaged over assimilation steps during the analysis period, the corresponding mean reductions are 0.16, 0.17, and 0.19, respectively. Within the YRD (Fig. S6h), uncertainty reduction is uneven, with the largest reductions over the central YRD and the eastern coast; the maximum occurs in Shanghai (0.41).

The sectoral maps show that the inversion reduces uncertainty primarily in the dominant-emitting sectors. Over the parent domain (Fig. S6b–g), the largest reduction for the rice cultivation sector is over the YRD, while the natural sector is best constrained over northern Japan (maximum 0.37), with a weaker signal over the YRD. For waste, the strongest reductions occur in Shanghai and South Korea. In contrast, sectors with smaller contributions show little and spatially scattered reductions, especially the "Other" sector, whose peak is only 0.06. A similar pattern is found within the YRD (Fig. S6i–n): uncertainty reduction is mainly concentrated in the rice cultivation, natural, waste, and fuel exploitation sectors, whereas the livestock and "Other" sectors remain weakly constrained.

To assess the robustness of posterior sectoral attribution over the YRD, we further examined Pearson correlations among YRD-integrated sector totals for each sector pair (Appendix B). Table B1 compares the unconstrained prior state at lag 1 with the final optimized posterior state at lag 0, together with the prior-to-posterior correlation shift. After inversion, correlations become more negative for almost all sector pairs, pointing to enhanced sectoral trade-offs in the posterior estimates. The largest shifts occur for Sector 1–2, Sector 1–3, and Sector 2–3, whose correlations decrease from -0.013, -0.008, and -0.013 in the prior state to -0.294, -0.214, and -0.158 in the posterior state, respectively. Outside these three pairs, the posterior correlations are generally weaker in magnitude.

Overall, within the YRD, the strongest uncertainty reductions occur in the central area and in the dominant emitting sectors, while changes are modest in peripheral areas and for minor sectors, given the current station network.

3.3 Real-data inversion in 2022: validation and comparison

3.3.1 Validation using independent measurements

Figure 11 presents the hourly time series of the prior and the posterior CH_4 concentrations, compared with independent observations (locations shown in Fig. S1). At the DMS station, the only in situ surface station used for independent evaluation, the simulation with prior estimates (red solid line) generally exhibits substantially higher concentration peaks than the optimized simulation (blue solid line) (Fig.

11a). Consistently, the posterior reduces the frequency of errors > 50 ppb (Fig. 11b). During late summer, particularly from August to September, the observed CH_4 concentrations remain notably higher than the simulations. The comparison with total-column observations indicates both smaller enhancements over background and smaller model-observation mismatches than for the surface site (Fig. 11c, e). Relative to SH, the HF errors are more tightly clustered within -30 to -10 ppb (Fig. 11d, f).

We quantify the agreement between simulations and independent observations using the MAE, root mean square error (RMSE), and correlation coefficient for both hourly and daily averaged CH_4 concentrations (Fig. 12). Overall, the optimized simulation reduces the model-observation mismatch at all three sites, although changes in temporal correlation differ between the surface and total-column observations. At the DMS station, the MAE decreases from 41.1 ppb to 38.0 ppb for hourly concentrations and from 30.9 ppb to 27.5 ppb for daily means, corresponding to reductions of 7.5% and 11.0%, respectively (Fig. 12a, d). The RMSE shows a similar improvement, decreasing from 56.4 to 52.0 ppb for hourly data and from 41.2 to 36.6 ppb for daily means, equivalent to reductions of 7.8% and 11.2% (Fig. 12b, e). Temporal correlation also improves at this site, with the correlation coefficient for daily means reaching 0.72 in the posterior case (Fig. 12c, f).

For the total-column measurements at the HF station, the posterior simulation improves the temporal correlation substantially, with the correlation coefficient increasing from 0.80 to 0.85 for hourly data and from 0.72 to 0.83 for daily means. In contrast, the error metrics change little: the hourly MAE increases slightly by 2.2 % (0.5 ppb), the daily MAE decreases marginally by 0.5 % (0.1 ppb), the hourly RMSE remains unchanged, and the daily RMSE decreases by 5.8 % (1.3 ppb). At the SH station, the response is nearly opposite. The inversion reduces the MAE by 18.3 % (3.2 ppb) for hourly concentrations and by 16.2 % (2.8 ppb) for daily means, yielding the largest relative improvement in hourly MAE among the three sites. The RMSE also declines by 16.4 % (3.7 ppb) for hourly data and by 14.0 % (3.1 ppb) for daily means, indicating a clear improvement in concentration magnitude. By contrast, the temporal correlation decreases after inversion.

Overall, independent validation with both total-column and surface observations indicates that the inversion reduces the model-observation mismatch, with generally stronger improvements at the surface sites than at the column sites. This is expected because the inversion is constrained only by surface observations, while total-column XCH_4 is less sensitive to near-surface flux perturbations than surface in situ observations. In addition, the lack of averaging-kernel treatment at SH (Sect. 2.4) may further weaken the model-observation consistency there. Nevertheless, the improved correlation at HF and the improved concentration magnitude at SH still suggest that the inversion captures part of the column response to the optimized surface fluxes.

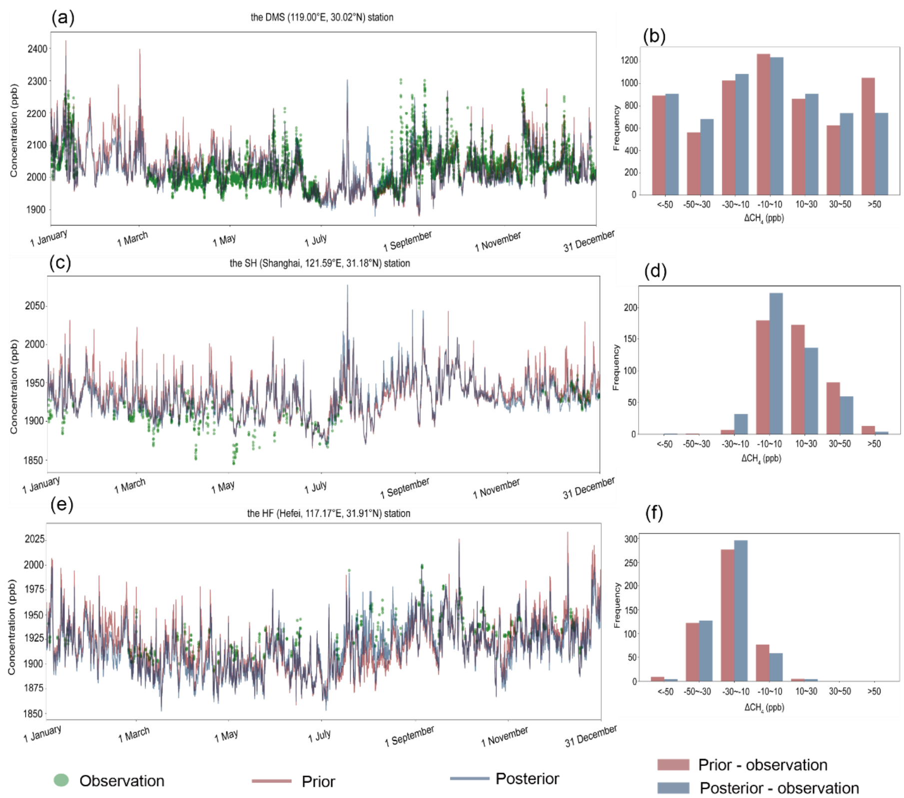

Figure 11: Hourly CH_4 concentrations (ppb) simulated with prior and posterior emissions, together with observations and the corresponding frequency distributions of hourly model errors (model minus observation), at the (a, b) DMS station, (c, d) SH (Shanghai) station, and (e, f) HF (Hefei) station in the YRD during 2022.

https://doi.org/10.5194/egusphere-2026-3879
Preprint. Discussion started: 27 July 2026

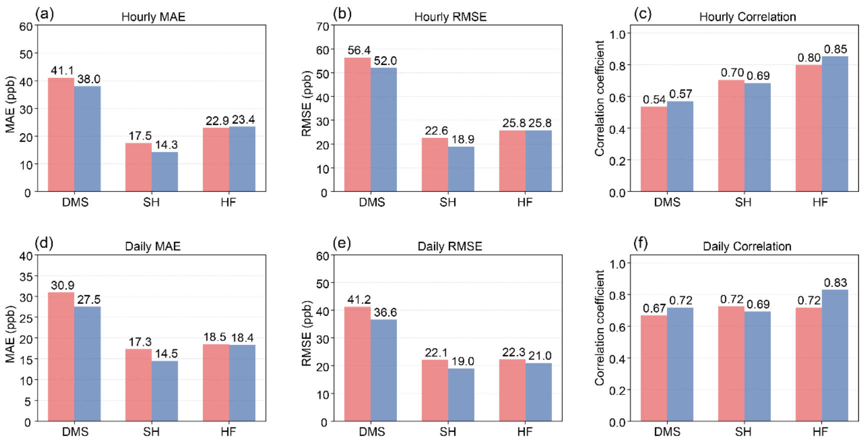

Figure 12: Statistics of hourly (a–c) and daily (d–f) CH_4 concentration differences between simulations driven by prior and posterior emissions and observations at three independent sites in the YRD, quantified by the (a, d) MAE (ppb), (b, e) root mean square error (RMSE, ppb), and (c, f) correlation coefficient.

3.3.2 Comparison of annual and monthly CH_4 emissions in the YRD

To further evaluate the inversion results, we compare emissions in observation-rich regions with those reported in previous studies and in existing inventories. For the posterior estimates, we present the ensemble mean and the standard deviation across all ensemble members. In the discussion below, we use the ensemble mean values. Regional totals for the prior and posterior emissions are calculated from the WRF-grid emission fields used in the inversion. External gridded products, including EDGAR, CEDS-2025 (Feng et al., 2020; Hoesly et al., 2018) and CAMS v6.2, are first mapped to the same WRF grid and then integrated over the corresponding regional boundaries. For NOAA's CarbonTracker-CH_4 (CT-CH4-2025, Oh et al., 2025) and CAMS inversion-optimized fluxes (CAMS v25r1; Bergamaschi et al., 2013), both provided at 1° × 1° resolution, regional totals are calculated using an area-weighted approach that accounts for partial overlaps between grid cells and the target region. All estimates are reported in Tg yr^{-1}.

Over the parent domain (Fig. 13a), the posterior total is 65.77 ± 0.74 Tg yr^{-1}, which is 3.54 Tg yr^{-1} (5.1%) lower than the prior total of 69.31 Tg yr^{-1}. The reduction is driven mainly by fuel exploitation (-1.53 Tg yr^{-1}) and waste (-1.14 Tg yr^{-1}), while rice cultivation, natural emissions, livestock, and the "Other" sector all decrease more modestly, by 0.44, 0.31, 0.09, and 0.03 Tg yr^{-1}, respectively. For anthropogenic emissions, the posterior anthropogenic total is 58.19 Tg yr^{-1}, 5.2% lower than the prior anthropogenic estimate (61.41 Tg yr^{-1}). Compared with other anthropogenic inventories, the posterior is lower than

https://doi.org/10.5194/egusphere-2026-3879
Preprint. Discussion started: 27 July 2026

EDGAR v8, EDGAR_2024, and CAMS v6.2 by 17.2%, 1.9%, and 7.9%, respectively, but higher than EDGAR_2025, Feng et al. (2025), and CEDS-2025 by 16.0%, 19.1%, and 14.1%, respectively. For total emissions, the posterior is 13.0% higher than CT-CH4-2025, but 18.0% lower than CAMS v25r1.

Within the YRD (Fig. 13b), the posterior total is 7.53 ± 0.09 Tg yr^{-1}, which is 0.93 Tg yr^{-1} (11.0%) lower than the prior total of 8.46 Tg yr^{-1}. The reduction is driven mainly by waste (-0.42 Tg yr^{-1}) and fuel exploitation (-0.26 Tg yr^{-1}). Rice cultivation also decreases noticeably by 0.21 Tg yr^{-1}, whereas the changes in livestock and the "Other" sector are much smaller (~ 0.01 Tg yr^{-1}). Natural emissions also decrease slightly by 0.03 Tg yr^{-1}. For anthropogenic totals, the posterior anthropogenic total is 6.18 Tg yr^{-1}, 12.7% lower than the prior anthropogenic estimate (7.09 Tg yr^{-1}). Compared with other anthropogenic estimates, the posterior is closest to CEDS-2025, differing by only 0.11 Tg yr^{-1} (1.7%). It is also close to EDGAR_2025, although it is 0.54 Tg yr^{-1} (9.7%) higher. In contrast, the posterior is lower than EDGAR v8, EDGAR_2024, CAMS v6.2, and Feng et al. (2025) by 31.2%, 19.8%, 20.9%, and 14.2%, respectively. At the sector level, EDGAR_2025 gives the lowest rice cultivation estimate, 1.74 Tg yr^{-1}, equivalent to 63.6% of the posterior rice CH_4 estimate. For total emissions, the posterior is 0.54 Tg yr^{-1} (6.7%) lower than CT-CH4-2025 and 2.40 Tg yr^{-1} (24.2%) lower than CAMS v25r1.

The monthly comparison of anthropogenic CH_4 emissions in the YRD (Fig. 13c) highlights clear differences in seasonal structure among datasets. The prior emissions remain nearly flat throughout the year, whereas the posterior emissions show a distinct summer enhancement, increasing from spring to a broad peak in July to August and then declining in autumn. Among the external inventories, EDGAR_2025 and CEDS-2025 are closest to the posterior. EDGAR_2025 best matches the posterior seasonal phase and amplitude, while CEDS-2025 shows weaker seasonal variability. EDGAR v8 and EDGAR_2024 show a similar seasonal tendency but with substantially higher summer emissions, while CAMS v6.2 remains comparatively flat and generally higher than the posterior emissions in most months. Feng et al. (2025) exhibits the strongest seasonality, with a much sharper August maximum than any other dataset.

Overall, the inversion reduces anthropogenic CH_4 emissions in the YRD relative to the prior. The posterior anthropogenic estimate is lower than EDGAR v8.0, EDGAR_2024, CAMS v6.2, and Feng et al. (2025), but close to EDGAR_2025 and CEDS-2025. The monthly comparison further indicates that the posterior captures a seasonal pattern broadly consistent with EDGAR_2025. For total emissions in the YRD, the posterior is lower than both CT-CH4-2025 and CAMS v25r1, with a larger difference relative to CAMS v25r1.

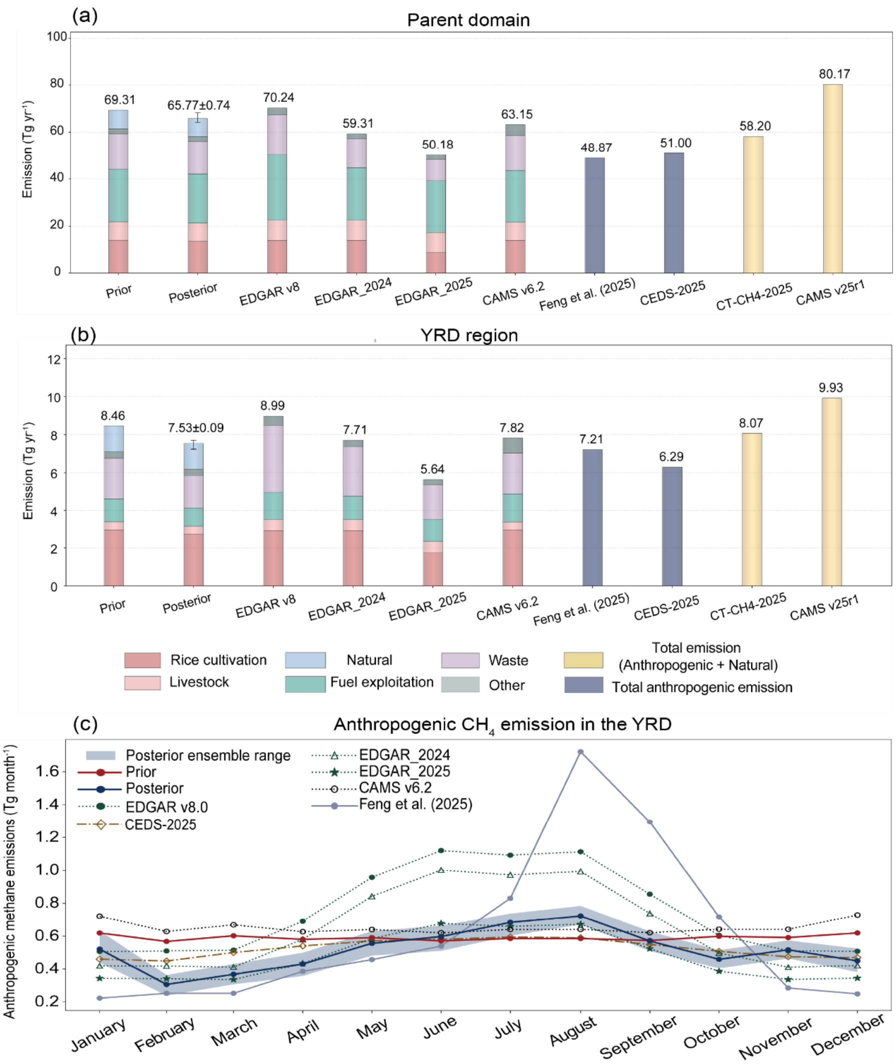

Figure 13: Annual total CH_4 emissions from different inventories and studies output across (a) the parent domain, (b) YRD region, and (c) monthly anthropogenic emissions in the YRD.

4 Conclusions and implications

This work establishes the first benchmark for the CTDAS-WRF regional inversion framework for CH_4 over key emission regions in East Asia, demonstrating its capability to constrain emissions using a limited in situ network. Through an OSSE, a combination of sensitivity tests and a full-year inversion for 2022 using real data, we evaluate the system's performance, characterize emission patterns in the Yangtze River Delta (YRD), and compare results against independent data and previously published emission estimates.

The OSSE demonstrates that a reference inversion setup can partially recover a prescribed uniform two-fold emission increase in the YRD (~61%), South Korea (~68%), and northern Japan (north of 37°N; ~93%) using a nine-site network. In contrast, domain-wide adjustments recover only 22.5% of the imposed emission adjustment, reflecting the limited spatial coverage of observations. Within the YRD, the strongest corrections are applied to emissions from natural sources, rice cultivation, waste and fuel, while weaker changes are observed for livestock, and the "Other" categories, consistent with their lower contribution to the total emissions. Meanwhile, the mean concentration mismatch decreases by ~59.5% (from 318ppb to 129 ppb). Inversion performance improves with larger ensembles, higher prior uncertainties, fewer flux categories, and more observation sites, but degrades with shorter localization scales (from 900 km to 600 km) and shorter assimilation windows (from 10 days to 5 days).

The 2022 inversion based on real in situ data indicates substantial sector- and subregional biases in prior YRD emissions, with anthropogenic hotspots generally overestimated and natural emissions, especially in southwestern Anhui, underestimated. Anhui has the largest total CH_4 emissions, with fuel exploitation overestimated by 0.22 Tg yr^{-1} (22.2%) and natural emissions underestimated by 0.07 Tg yr^{-1} (12.9%), whereas Jiangsu shows the largest waste reduction (0.15 Tg yr^{-1}, 19.5%). Shanghai is characterized by overestimated waste and fuel exploitation (0.08 Tg yr^{-1}, 33.1%; 0.02 Tg yr^{-1}, 17.9%), while Zhejiang shows reductions in rice cultivation and waste (0.08 Tg yr^{-1}, 9.4%; 0.11 Tg yr^{-1}, 21.1%).

Temporally, the posterior fluxes in the YRD exhibit a pronounced summer maximum peaking in August, with adjustments ranging from -52.1% to +61.0%. The seasonal amplitude of the posterior emissions (~0.03 Gg) is about one order of magnitude larger than that of the prior. The prior underestimation is driven mainly by natural emissions and rice cultivation, which contribute 41.7% (0.35 Tg) and 40.4% (0.34 Tg), respectively, whereas annual overestimation is dominated by waste and fuel exploitation, with waste contributing 26.7% (0.47 Tg) and fuel exploitation 17.8% (0.32 Tg). These results highlight the importance of accurately representing the spatiotemporal variability for understanding emissions.

https://doi.org/10.5194/egusphere-2026-3879
Preprint. Discussion started: 27 July 2026

The posterior total emission for the YRD is 7.53 ± 0.09 Tg yr^{-1}, 11.0% lower than the prior estimate of 8.46 Tg yr^{-1}. The posterior anthropogenic emission is 6.18 Tg yr^{-1}, lower than EDGAR v8.0, EDGAR_2024, CAMS v6.2, and Feng et al. (2025) by 31.2%, 19.8%, 20.9%, and 14.2%, respectively, but close to CEDS-2025 (1.7%) and higher than EDGAR_2025 by 9.7%. For the total YRD budget, the posterior is 0.54 Tg yr^{-1} (6.7%) lower than CT-CH4-2025 and 2.40 Tg yr^{-1} (24.2%) lower than CAMS v25r1. The monthly comparison further shows that the posterior captures a clear summer enhancement, with EDGAR_2025 closest in seasonal phase and amplitude, whereas CEDS-2025 is closer in annual magnitude but has weaker seasonality. Overall, the inversion suggests lower YRD anthropogenic CH_4 emissions than most existing inventories, while highlighting the importance of both annual magnitude and seasonal structure in inventory evaluation.

Independent evaluation against surface and total-column observations confirms an overall posterior improvement. At DMS, the inversion reduces MAE and RMSE by 7.5%–11.2%, and improves the daily correlation to 0.72. At HF, the main improvement is in temporal correlation, increasing from 0.80 to 0.85 for hourly data and from 0.72 to 0.83 for daily means, while error metrics change little. At SH, MAE and RMSE decrease by 14.0%–18.3%, although temporal correlation declines. These results indicate that the posterior simulation better matches independent observations than the prior, with different responses at surface and total-column sites.

Several limitations warrant consideration. First, our OSSE (Observing System Simulation Experiments) employs a "true" emission pattern that scales the prior spatial pattern uniformly, which does not test the system's ability to correct spatially complex, heterogeneous errors. This pattern is intentionally simpler than the spatially heterogeneous perturbations used elsewhere, such as random Gaussian fields (Steiner et al., 2024), making it a practical starting point to facilitate interpretation. Consequently, the inferred performance may not fully generalize to more realistic prior-true-state mismatches. Second, the sensitivity design is not exhaustive; repeated perturbations for individual parameters and more systematic testing are required to fully assess robustness and parameter interactions. Third, the YRD is constrained by mainly two sites (Nanjing and Shanghai), both in the northern/eastern part of the region. This network leaves northwestern hotspots, especially fuel exploitation and livestock, less constrained, leading to weaker adjustments and smaller uncertainty reductions than for better-observed sectors (waste, natural, rice cultivation). In addition, posterior inter-sector coupling over the YRD is generally weak, but residual trade-offs remain among rice cultivation, natural, and waste sectors.

In conclusion, our results establish a foundation for future longer-term inversions that integrate multiple observing systems, including additional in situ sites and satellite column observations. Expanding observational coverage, particularly in under-constrained source regions, will enable more rigorous cross-comparisons and a more complete understanding of the CH_4 budget across East Asia.

Code and data availability

TCCON data are obtained from the TCCON Data Archive hosted by CaltechDATA (https://tccondata.org, last access: 12 March 2026). CarbonTracker-CH4 (CT-CH4-2025) results are obtained from NOAA GML (https://gml.noaa.gov/ccgg/carbontracker-ch4/, last access: 12 March 2026). ERA5 meteorological data are obtained from the C3S Climate Data Store, including hourly data on single levels (https://doi.org/10.24381/cds.adbb2d47) and pressure levels (https://doi.org/10.24381/cds.bd0915c6; last access: 26 March 2026). CAMS inversion-optimised greenhouse gas fluxes and concentrations and CAMS global emission inventories are obtained from the CAMS Atmosphere Data Store (https://doi.org/10.24381/ed2851d2 and https://doi.org/10.24381/1d158bec; last access: 26 March 2026). Ocean and land raster data are obtained from the GEBCO 2024 Grid (https://doi.org/10.5285/1c44ce99-0a0d-5f4f-e063-7086abc0ea0f). Administrative boundaries are obtained from GADM (https://gadm.org/about.html), with Chinese boundary references from the Aliyun database (https://datav.aliyun.com/portal/school/atlas/area_selector). The GRPI rice CH_4 inventory was obtained from Zenodo (Chen and Jacob, 2025; https://doi.org/10.5281/zenodo.15210212), and CEDS-2025 was obtained from the input4MIPs/CMIP7 CEDS product (https://doi.org/10.5281/zenodo.15001546). The CTDAS-WRF code is available from https://git.wur.nl/ctdas/CTDAS/-/tree/ctdas-wrf. WRF-Chem is available from https://github.com/wrf-model. The posterior emission estimates and simulated concentration fields from this study will be made publicly available through Zenodo upon publication.

Author contributions

ML, HC, and SH conceived and designed the research. WP and FR developed the CTDAS-WRF inversion system. ML conducted the simulations, analyzed the data, and wrote the manuscript. FW generated the key flux data, and XC, CW, and SF conducted the key observational work. FR, SH, XZ, and EI provided technical guidance and training support. HC, XZ, FW, EI, FR, XW, PP, WP, KH, and SH reviewed and commented on the manuscript. HC, KH, and SH supervised the project.

Competing interests

At least one of the (co-)authors is a member of the editorial board of Atmospheric Chemistry and Physics.

https://doi.org/10.5194/egusphere-2026-3879
Preprint. Discussion started: 27 July 2026

Acknowledgments

This work uses the Dutch national e-infrastructure with the support of the SURF Cooperative under grants no. EINF-8215 and EINF-14758. We also acknowledge the NWO (SURF) small compute grant and the use of computing resources at the SURF HPC centre (Snellius), which provides the computational capacity for this study. We thank the World Data Centre for Greenhouse Gases (WDCGG) and its data contributors, including the Japan Meteorological Agency (JMA), the Korea Meteorological Administration (KMA), and the National Institute for Environmental Studies (NIES), for providing access to the surface atmospheric CH_4 datasets used in this study. We gratefully acknowledge Prof. Aijun Ding from Nanjing University for providing the key observational dataset used in this study.

Appendix A. Inversion methodology

The CTDAS system applies an Ensemble Kalman Filter (EnKF) to simultaneously optimize CH_4 fluxes and background parameters by minimizing a cost function J, within a fixed assimilation window (He et al., 2018; Peters et al., 2005, 2007, 2010; Steiner et al., 2024; van der Laan-Luijkx et al., 2017):

$$J(x) = \left(y^o - \mathcal{H}(x)\right)^{\mathrm{T}} \mathbf{R}^{-1} \left(y^o - \mathcal{H}(x)\right) + (x - x^b)^{\mathrm{T}} \mathbf{P}^{-1} (x - x^b), \tag{A1}$$

Here, y^o represents the atmospheric CH_4 mole fraction observations and **R** denotes the observation-error covariance matrix. **R** is prescribed as a diagonal matrix whose diagonal elements are the squared model-data mismatch values assigned to individual observations. The observation operator $\mathcal{H}$, which maps the state vector x to the observation space, represents a WRF-Chem model simulation. The state vector x includes surface CH_4 fluxes and boundary conditions. x^b and **P** denote the prior state vector and its prior error covariance matrix, respectively. The EnKF represents the uncertainty of the state vector by an ensemble of model states rather than by explicitly propagating a full prior error covariance matrix. The ensemble statistics are then used to estimate the covariance of the state vector and to sequentially update the state vector as new observations become available (Feng et al., 2025; Tsuruta, 2017b).

An ensemble of n = 100 members ($i \in \{1, 2, 3\ldots, 100\}$) is used to represent the prior uncertainty in the state vector. In CTDAS, the first member is set equal to the mean state ($\bar{x}^b = x_1^b$), while the remaining members represent perturbations around it. Thus, each ensemble member is written as:

$$x_i^b = \bar{x}^b + x_i'^b, \tag{A2}$$

https://doi.org/10.5194/egusphere-2026-3879
Preprint. Discussion started: 27 July 2026

where $\bar{x}^b$ and $x_i^b \in \mathbf{R}^{N_s}$, are N_s-dimensional state vectors, and $x_i'^b$ denotes the corresponding perturbation. The state-space ensemble perturbation matrix is then defined as:

$$\mathbf{X}^b = \frac{1}{\sqrt{n-1}}[x_2^b - \bar{x}^b, \dots, x_n^b - \bar{x}^b], \tag{A3}$$

The corresponding prior error covariance ($\mathbf{P}^{\boldsymbol{b}}$) is represented implicitly by the ensemble as:

$$\mathbf{P}^{\boldsymbol{b}} = \mathbf{X}^b(\mathbf{X}^b)^{\boldsymbol{T}}, \tag{A4}$$

Using the state-space ensemble defined above, the corresponding ensemble in observation space is obtained by applying the observation operator $\mathcal{H}$ (WRF-Chem) to each ensemble member, i.e. by sampling the simulated concentrations at the observation times and locations. Accordingly, the simulated observation of ensemble member *i* is:

$$y_i^b = \mathcal{H}(x_i^b), \tag{A5}$$

Here, $y_1^b = \bar{y}^b$ denotes the simulated observation corresponding to the mean state $\bar{x}^b$, whereas y_i^b represents the simulated observations from the perturbed ensemble members. The corresponding observation-space perturbation matrix is:

$$\mathbf{Y}^b = \frac{1}{\sqrt{n-1}}[y_2^b - \bar{y}^b, \dots, y_n^b - \bar{y}^b], \tag{A6}$$

From these matrices, the state–observation cross-covariance and the observation-space covariance are estimated as:

$$\mathbf{P}_{xy}^b = \mathbf{X}^b(\mathbf{Y}^b)^{\boldsymbol{T}}, \tag{A7}$$

$$\mathbf{P}_{yy}^b = \mathbf{Y}^b(\mathbf{Y}^b)^{\boldsymbol{T}}, \tag{A8}$$

The Kalman gain matrix **G** is then computed as:

$$\mathbf{G} = \mathbf{P}_{xy}^b\,(\mathbf{P}_{yy}^b + \mathbf{R})^{-1}, \tag{A9}$$

For the ensemble mean, the analysis update is:

$$\bar{x}^a = \bar{x}^b + \mathbf{G}\,(\mathrm{y}^o - \mathcal{H}(\bar{x}^b)), \tag{A10}$$

The ensemble perturbations are updated separately following the ensemble square root filter formulation (Peters et al., 2005), and the posterior ensemble members are reconstructed from the updated mean and

https://doi.org/10.5194/egusphere-2026-3879
Preprint. Discussion started: 27 July 2026

updated perturbations as:

$$x_i^a = \bar{x}^a + x_i'^a, \tag{A11}$$

Particularly, for an assimilated observation j, the corresponding perturbation update can be written as:

$$x_{i,j}'^a = x_{i,j}'^b + \alpha_j g_j Y_j^b, \tag{A12}$$

where Y_j^b denotes the j-th row of the observation-space perturbation matrix $\mathbf{Y}^b$, vector g_j is the Kalman gain for observation j, α_j is the square-root factor as:

$$\alpha_j = (1 + \sqrt{\frac{R_j}{P_{yy,j}^b + R_j}})^{-1}, \tag{A13}$$

where $P_{yy,j}^b$ is the prior ensemble variance for observation j and R_j is the observation error variance for observation j.

Here, x^a denotes the optimized state vector. The detailed optimization procedure is illustrated in Fig. 2.

Appendix B. Annual mean posterior inter-sector correlation in the YRD

We examine correlations of YRD-integrated sector totals and their shifts from the prior to the posterior state in Table B1. For each assimilation cycle c, lag l, sector p, region element e, and ensemble member i, the prior and posterior scaling factors are reconstructed as:

$$\lambda_{c,l,p,e,i}^b = \bar{\lambda}_{c,l,p,e,i}^b + \lambda_{c,l,p,e,i}'^b, \tag{B5}$$

$$\lambda_{c,l,p,e,i}^a = \bar{\lambda}_{c,l,p,e,i}^a + \lambda_{c,l,p,e,i}'^a, \tag{B6}$$

where $\bar{\lambda}^b$ and $\bar{\lambda}^a$ are the prior and posterior ensemble means, λ'^b and λ'^a are the corresponding ensemble perturbations.

The corresponding prior and posterior YRD-integrated sector totals are then computed as:

$$E_{c,l,p,i}^b = \sum_{e \in B_p^{YRD}} \lambda_{c,l,p,e,i}^b F_{c,l,p,e}^b, \tag{B7}$$

$$E_{c,l,p,i}^a = \sum_{e \in B_p^{YRD}} \lambda_{c,l,p,e,i}^a F_{c,l,p,e}^a, \tag{B8}$$

where B_p^{YRD} denotes the set of YRD state-vector elements belonging to sector p, and $F_{c,l,p,e}^b$ is the prior sectoral flux integrated over the corresponding lag window and YRD grid cells assigned to region

https://doi.org/10.5194/egusphere-2026-3879
Preprint. Discussion started: 27 July 2026

element e.

For any two sectors p and q, the prior and posterior inter-sector correlations are then computed as Pearson correlation coefficients across ensemble members:

$$C^b_{c,l}(p,q) = \frac{cov\,(E^b_{c,l,p}, E^b_{c,l,q})}{\sigma(E^b_{c,l,p})\sigma(E^b_{c,l,q})}, \tag{B9}$$

$$C^a_{c,l}(p,q) = \frac{cov\,(E^a_{c,l,p}, E^a_{c,l,q})}{\sigma(E^a_{c,l,p})\sigma(E^a_{c,l,q})}, \tag{B10}$$

where $cov\,(\cdot,\cdot)$ denotes the covariance and $\sigma(\cdot)$ is the ensemble standard deviation of the corresponding YRD-integrated sector totals. The prior-to-posterior change in YRD-integrated sector coupling is quantified as:

$$\Delta C_c(p,q) = C^a_{c,0}(p,q) - C^b_{c,1}(p,q), \tag{B11}$$

Annual mean values are obtained by averaging $C^a_{c,0}(p,q), C^b_{c,1}(p,q)$ over all assimilation cycles. Here, the prior state at lag = 1 corresponds to the case with a scaling factor of 1 applied at the input stage (Fig. 2), i.e., before any observational constraint is imposed, whereas the posterior state at lag = 0 represents the final optimized result after assimilation of the observations. This aggregated-sector diagnostic provides a strict test of source separability at the regional-total scale.

Table B1. Annual-mean Pearson correlation coefficients of YRD-integrated sector totals for each sector pair, shown for the prior state at lag 1 and the posterior state at lag 0, together with the correlation shift from prior to posterior.

Sector pair	C^b (lag 1)	C^a (lag 0)	ΔC
Sector 1, 2	-0.013	-0.294	-0.281
Sector 1, 3	-0.008	-0.214	-0.206
Sector 1, 4	0.004	-0.021	-0.025
Sector 1, 5	-0.010	-0.021	-0.011
Sector 1, 6	0.016	-0.022	-0.038
Sector 2, 3	-0.013	-0.158	-0.145
Sector 2, 4	0.008	-0.032	-0.04
Sector 2, 5	0.000	-0.007	-0.007

https://doi.org/10.5194/egusphere-2026-3879
Preprint. Discussion started: 27 July 2026

Sector 2, 6	0.029	-0.005	-0.034
Sector 3, 4	0.000	-0.052	-0.052
Sector 3, 5	-0.001	-0.017	-0.016
Sector 3, 6	0.013	-0.055	-0.068
Sector 4, 5	0.022	0.001	-0.021
Sector 4, 6	0.014	0.005	-0.009
Sector 5, 6	0.025	0.023	-0.002

References

Ai, X., Hu, C., Yang, Y., Zhang, L., Liu, H., Zhang, J., Chen, X., Bai, G., and Xiao, W.: Quantification of Central and Eastern China's atmospheric CH_4 enhancement changes and its contributions based on machine learning approach, J. Environ. Sci., 138, 236–248, https://doi.org/10.1016/j.jes.2023.03.010, 2024.

Beck, V., Koch, T., Kretschmer, R., Marshall, J., Ahmadov, R., Gerbig, C., Pillai, D., and Heimann, M.: The WRF Greenhouse Gas Model (WRF-GHG), Tech. Rep. 25, Max Planck Institute for Biogeochemistry, Jena, Germany, https://www.bgc-jena.mpg.de/bgc-systems/uploads/Wrf-ghg/Technical Reports 2011 Beck.pdf, last access: 12 March 2026, 2011.

Bergamaschi, P., Houweling, S., Segers, A., Krol, M., Frankenberg, C., Scheepmaker, R. A., Dlugokencky, E., Wofsy, S. C., Kort, E. A., Sweeney, C., Schuck, T., Brenninkmeijer, C., Chen, H., Beck, V., and Gerbig, C.: Atmospheric CH_4 in the first decade of the 21st century: Inverse modeling analysis using SCIAMACHY satellite retrievals and NOAA surface measurements, J. Geophys. Res. Atmos., 118, 7350–7369, https://doi.org/10.1002/jgrd.50480, 2013.

Brasseur, G. P. and Jacob, D. J.: Modeling of atmospheric chemistry, Cambridge University Press, Cambridge, ISBN 978-1-107-14696-9, 2017.

Cai, B., Lou, Z., Wang, J., Geng, Y., Sarkis, J., Liu, J., and Gao, Q.: CH_4 mitigation potentials from China landfills and related environmental co-benefits, Sci. Adv., 4, eaar8400, https://doi.org/10.1126/sciadv.aar8400, 2018.

https://doi.org/10.5194/egusphere-2026-3879
Preprint. Discussion started: 27 July 2026

Callewaert, S.: User guide for the greenhouse gas option of WRF-Chem (WRF-GHG), version 1.0, https://doi.org/10.18758/Q6RAPNEU, 2024.

Chen, D., Ma, M., Hu, L., Du, Q., Li, B., Yang, Y., Guo, L., Cai, Z., Ji, M., Zhu, R., and Fang, X.: Characteristics of China's coal mine methane emission sources at national and provincial levels, Environ. Res., 259, 119549, https://doi.org/10.1016/j.envres.2024.119549, 2024.

Chen, H., Zhu, Q., Peng, C., Wu, N., Wang, Y., Fang, X., Jiang, H., Xiang, W., Chang, J., Deng, X., and Yu, G.: Methane emissions from rice paddies, natural wetlands, and lakes in China: synthesis and new estimate, Glob. Change Biol., 19, 19–32, https://doi.org/10.1111/gcb.12034, 2013.

Chen, S.-H. and Sun, W.-Y.: A one-dimensional time dependent cloud model, J. Meteorol. Soc. Jpn., 80, 99–118, https://doi.org/10.2151/jmsj.80.99, 2002.

Chen, Z., Jacob, D. J., Nesser, H., Sulprizio, M. P., Lorente, A., Varon, D. J., Lu, X., Shen, L., Qu, Z., Penn, E., and Yu, X.: Methane emissions from China: a high-resolution inversion of TROPOMI satellite observations, Atmos. Chem. Phys., 22, 10809–10826, https://doi.org/10.5194/acp-22-10809-2022, 2022.

Chen, Z., Lin, H., Balasus, N., Hardy, A., East, J. D., Zhang, Y., Runkle, B. R. K., Hancock, S. E., Taylor, C. A., Du, X., Sander, B. O., and Jacob, D. J.: Global Rice Paddy Inventory (GRPI): a high-resolution inventory of methane emissions from rice agriculture based on Landsat satellite inundation data, Earth's Future, 13, e2024EF005479, https://doi.org/10.1029/2024EF005479, 2025.

Colligan, T., Poulter, B., and Quinn, C.: LPJ-EOSIM L2 Global Simulated Daily Wetland Methane Flux Low Latency V001, NASA Land Processes Distributed Active Archive Center [data set], https://doi.org/10.5067/COMMUNITY/LPJ-EOSIM/LPJ_EOSIM_L2_DCH4E_LL.001, last access: 13 March 2026, 2024.

Crippa, M., Guizzardi, D., Schaaf, E., Monforti-Ferrario, F., Quadrelli, R., Risquez Martin, A., Rossi, S., Vignati, E., Muntean, M., Brandao De Melo, J., Oom, D., Pagani, F., Banja, M., Taghavi-Moharamli, P., Köykkä, J., Grassi, G., Branco, A., and San-Miguel, J.: GHG emissions of all world countries - 2023, Publications Office of the European Union, ISBN 978-92-68-07550-0, ISSN 1831–9424, Catalogue number KJ-NA-31-658-EN-N, https://doi.org/10.2760/953322, 2023.

Crippa, M., Guizzardi, D., Pagani, F., Banja, M., Muntean, M., Schaaf, E., Monforti-Ferrario, F., Becker,

https://doi.org/10.5194/egusphere-2026-3879
Preprint. Discussion started: 27 July 2026

W. E., Quadrelli, R., Risquez Martin, A., Taghavi-Moharamli, P., Köykkä, J., Grassi, G., Rossi, S., Melo, J., Oom, D., Branco, A., San-Miguel, J., Manca, G., Pisoni, E., Vignati, E., and Pekar, F.: GHG emissions of all world countries, Publications Office of the European Union, Luxembourg, JRC138862, https://doi.org/10.2760/4002897, 2024.

Crippa, M., Guizzardi, D., Pagani, F., Banja, M., Muntean, M., Schaaf, E., Quadrelli, R., Risquez Martin, A., Taghavi-Moharamli, P., Köykkä, J., Grassi, G., Melo, J., Suárez-Moreno, M., Sedano, F., San-Miguel, J., Manca, G., Pisoni, E., Pekar, F.: GHG emissions of all world countries, Publications Office of the European Union, Luxembourg, JRC143227, https://doi.org/10.2760/9816914, 2025.

Danielson, J. J. and Gesch, D. B.: Global multi-resolution terrain elevation data 2010 (GMTED2010), U.S. Geol. Surv., Open-File Rep. 2011–1073, iv, 23 pp., https://doi.org/10.3133/ofr20111073, 2011.

Ding, A. J., Fu, C. B., Yang, X. Q., Sun, J. N., Zheng, L. F., Xie, Y. N., Herrmann, E., Nie, W., Petäjä, T., Kerminen, V.-M., and Kulmala, M.: Ozone and fine particle in the western Yangtze River Delta: an overview of 1 yr data at the SORPES station, Atmos. Chem. Phys., 13, 5813–5830, https://doi.org/10.5194/acp-13-5813-2013, 2013.

Ding, A., Nie, W., Huang, X., Chi, X., Sun, J., Kerminen, V.-M., Xu, Z., Guo, W., Petäjä, T., Yang, X., Kulmala, M., and Fu, C.: Long-term observation of air pollution-weather/climate interactions at the SORPES station: a review and outlook, Front. Environ. Sci. Eng., 10, 15, https://doi.org/10.1007/s11783-016-0877-3, 2016.

East, J. D., Jacob, D. J., Balasus, N., Bloom, A. A., Bruhwiler, L., Chen, Z., Kaplan, J. O., Mickley, L. J., Mooring, T. A., Penn, E., Poulter, B., Sulprizio, M. P., Worden, J. R., Yantosca, R. M., and Zhang, Z.: Interpreting the seasonality of atmospheric methane, Geophys. Res. Lett., 51, e2024GL108494, https://doi.org/10.1029/2024GL108494, 2024.

Estrada, L. A., Varon, D. J., Sulprizio, M., Nesser, H., Chen, Z., Balasus, N., Hancock, S. E., He, M., East, J. D., Mooring, T. A., Oort Alonso, A., Maasakkers, J. D., Aben, I., Baray, S., Bowman, K. W., Worden, J. R., Cardoso-Saldaña, F. J., Reidy, E., and Jacob, D. J.: Integrated Methane Inversion (IMI) 2.0: an improved research and stakeholder tool for monitoring total methane emissions with high resolution worldwide using TROPOMI satellite observations, Geosci. Model Dev., 18, 3311–3330, https://doi.org/10.5194/gmd-18-3311-2025, 2025.

https://doi.org/10.5194/egusphere-2026-3879
Preprint. Discussion started: 27 July 2026

Etiope, G., Ciotoli, G., Schwietzke, S., and Schoell, M.: Gridded maps of geological methane emissions and their isotopic signature, Earth Syst. Sci. Data, 11, 1–22, https://doi.org/10.5194/essd-11-1-2019, 2019.

European Commission, Joint Research Centre (JRC), and International Energy Agency (IEA): EDGAR (Emissions Database for Global Atmospheric Research) Community GHG Database, comprising IEA-EDGAR CO_2, EDGAR CH_4, EDGAR N_2O, and EDGAR F-gases, version 2024, dataset, available at: https://edgar.jrc.ec.europa.eu/dataset_ghg2024, last access: 13 March 2026, 2024.

Fairall, C. W., Bradley, E. F., Hare, J. E., Grachev, A. A., and Edson, J. B.: Bulk parameterization of air–sea fluxes: updates and verification for the COARE algorithm, J. Climate, 16, 571–591, https://doi.org/10.1175/1520-0442(2003)016<0571:BPOASF>2.0.CO;2, 2003.

Feng, L., Smith, S. J., Braun, C., Crippa, M., Gidden, M. J., Hoesly, R., Klimont, Z., van Marle, M., van den Berg, M., and van der Werf, G. R.: The generation of gridded emissions data for CMIP6, Geosci. Model Dev., 13, 461–482, https://doi.org/10.5194/gmd-13-461-2020, 2020.

Feng, S., Jiang, F., Zhang, Y., Chen, H., Zhuang, H., Wang, S., Bai, S., Wang, H., and Ju, W.: High-resolution regional inversion reveals overestimation of anthropogenic methane emissions in China, Atmos. Chem. Phys., 25, 15121–15143, https://doi.org/10.5194/acp-25-15121-2025, 2025.

GMP: Global Methane Pledge, https://www.globalmethanepledge.org/resources/global-methane-pledge, last access: 12 March 2026, 2023.

Granier, C., Darras, S., Denier van der Gon, H., Doubalova, J., Elguindi, N., Galle, B., Gauss, M., Guevara, M., Jalkanen, J.-P., Kuenen, J., Liousse, C., Quack, B., Simpson, D., and Sindelarova, K.: The Copernicus Atmosphere Monitoring Service global and regional emissions (April 2019 version), Copernicus Atmosphere Monitoring Service (CAMS) report, https://doi.org/10.24380/d0bn-kx16, 2019.

Grell, G. A.: Prognostic evaluation of assumptions used by cumulus parameterizations, Mon. Weather Rev., 121, 764–787, https://doi.org/10.1175/1520-0493(1993)121<0764:PEOAUB>2.0.CO;2, 1993.

Grell, G. A. and Dévényi, D.: A generalized approach to parameterizing convection combining ensemble and data assimilation techniques, Geophys. Res. Lett., 29, 38-1–38-4, https://doi.org/10.1029/2002GL015311, 2002.

Grell, G. A., Peckham, S. E., Schmitz, R., McKeen, S. A., Frost, G., Skamarock, W. C., and Eder, B.:

https://doi.org/10.5194/egusphere-2026-3879
Preprint. Discussion started: 27 July 2026

Fully coupled "online" chemistry within the WRF model, Atmos. Environ., 39, 6957-6975, https://doi.org/10.1016/j.atmosenv.2005.04.027 , 2005.

Guo, F., Dai, F., Gong, P., and Zhou, Y.: CHN-CH4: a gridded (0.1° × 0.1°) anthropogenic methane emission inventory of China from 1990 to 2020, Earth Syst. Sci. Data, 17, 4799–4819, https://doi.org/10.5194/essd-17-4799-2025, 2025.

He, W., van der Velde, I. R., Andrews, A. E., Sweeney, C., Miller, J., Tans, P., van der Laan-Luijkx, I. T., Nehrkorn, T., Mountain, M., Ju, W., Peters, W., and Chen, H.: CTDAS-Lagrange v1.0: a high-resolution data assimilation system for regional carbon dioxide observations, Geosci. Model Dev., 11, 3515–3536, https://doi.org/10.5194/gmd-11-3515-2018, 2018.

He, Z., Gao, L., Liang, M., and Zeng, Z.-C.: A survey of methane point source emissions from coal mines in Shanxi province of China using AHSI on board Gaofen-5B, Atmos. Meas. Tech., 17, 2937–2956, https://doi.org/10.5194/amt-17-2937-2024, 2024.

Hersbach, H., Bell, B., Berrisford, P., Biavati, G., Horányi, A., Muñoz Sabater, J., Nicolas, J., Peubey, C., Radu, R., Rozum, I., Schepers, D., Simmons, A., Soci, C., Dee, D., and Thépaut, J.-N.: ERA5 hourly data on single levels from 1940 to present, Copernicus Climate Change Service (C3S) Climate Data Store (CDS) [data set], https://doi.org/10.24381/cds.adbb2d47, last access: 12 March 2026, 2023a.

Hersbach, H., Bell, B., Berrisford, P., Biavati, G., Horányi, A., Muñoz Sabater, J., Nicolas, J., Peubey, C., Radu, R., Rozum, I., Schepers, D., Simmons, A., Soci, C., Dee, D., and Thépaut, J.-N.: ERA5 hourly data on pressure levels from 1940 to present, Copernicus Climate Change Service (C3S) Climate Data Store (CDS) [data set], https://doi.org/10.24381/cds.bd0915c6, last access: 12 March 2026, 2023b.

Hoesly, R. M., Smith, S. J., Feng, L., Klimont, Z., Janssens-Maenhout, G., Pitkanen, T., Seibert, J. J., Vu, L., Andres, R. J., Bolt, R. M., Bond, T. C., Dawidowski, L., Kholod, N., Kurokawa, J.-I., Li, M., Liu, L., Lu, Z., Moura, M. C. P., O'Rourke, P. R., and Zhang, Q.: Historical (1750–2014) anthropogenic emissions of reactive gases and aerosols from the Community Emissions Data System (CEDS), Geosci. Model Dev., 11, 369–408, https://doi.org/10.5194/gmd-11-369-2018, 2018.

Houtekamer, P. L. and Mitchell, H. L.: Data Assimilation Using an Ensemble Kalman Filter Technique, Mon. Weather Rev., 126, 796–811, https://doi.org/10.1175/1520-

0493(1998)126<0796:DAUAEK>2.0.CO;2, 1998.

Hong, S.-Y., Noh, Y., and Dudhia, J.: A new vertical diffusion package with an explicit treatment of entrainment processes, Mon. Weather Rev., 134, 2318–2341, https://doi.org/10.1175/MWR3199.1, 2006.

Hu, C., Zhang, J., Qi, B., Du, R., Xu, X., Xiong, H., Liu, H., Ai, X., Peng, Y., and Xiao, W.: Global warming will largely increase waste treatment CH_4 emissions in Chinese megacities: insight from the first city-scale CH_4 concentration observation network in Hangzhou, China, Atmos. Chem. Phys., 23, 4501–4520, https://doi.org/10.5194/acp-23-4501-2023, 2023.

Hu, C., Zhang, Y., Yang, W., Wu, Y., Peng, T., Yang, Z., Han, C., Griffis, T. J., Hu, N., and Xiao, W.: Atmospheric inversion approach-based constraint on CH_4 emissions and future projections under climate scenarios for waste treatment: a case study in Yangtze River Delta region, China, J. Geophys. Res.-Atmos., 131, e2025JD044866, https://doi.org/10.1029/2025JD044866, 2026.

Huang, W., Griffis, T. J., Hu, C., Xiao, W., and Lee, X.: Seasonal variations of CH_4 emissions in the Yangtze River Delta region of China are driven by agricultural activities, Adv. Atmos. Sci., 38, 1537–1551, https://doi.org/10.1007/s00376-021-0383-9, 2021.

Iacono, M. J., Delamere, J. S., Mlawer, E. J., Shephard, M. W., Clough, S. A., and Collins, W. D.: Radiative forcing by long-lived greenhouse gases: Calculations with the AER radiative transfer models, J. Geophys. Res.-Atmos., 113, D13103, https://doi.org/10.1029/2008JD009944, 2008.

Ioannidis, E., Meesters, A., Steiner, M., Brunner, D., Reum, F., Pison, I., Berchet, A., Thompson, R., Sollum, E., Koch, F.-T., Gerbig, C., Wang, F., Maksyutov, S., Tsuruta, A., Tenkanen, M., Aalto, T., Monteil, G., Lin, H., Ren, G., Scholze, M., and Houweling, S.: An intercomparison of inverse models for estimating European CH_4 emissions, Earth Syst. Sci. Data, 18, 167–198, https://doi.org/10.5194/essd-18-167-2026, 2026.

IPCC: 2006 IPCC Guidelines for National Greenhouse Gas Inventories, prepared by the National Greenhouse Gas Inventories Programme, edited by: Eggleston, H. S., Buendia, L., Miwa, K., Ngara, T., and Tanabe, K., IGES, Japan, 2006.

Ito, A.: Output data of greenhouse gas budget and carbon cycle simulated by the VISIT terrestrial ecosystem model, ver.2023.2, NIES [data set], https://doi.org/10.17595/20210521.001, reference date:

2026/03/13, 2021.

Jiménez, P. A., Dudhia, J., González-Rouco, J. F., Navarro, J., Montávez, J. P., and García-Bustamante, E.: A revised scheme for the WRF surface layer formulation, Mon. Weather Rev., 140, 898–918, https://doi.org/10.1175/MWR-D-11-00056.1, 2012.

Kaiser, J. W., Heil, A., Andreae, M. O., Benedetti, A., Chubarova, N., Jones, L., Morcrette, J.-J., Razinger, M., Schultz, M. G., Suttie, M., and van der Werf, G. R.: Biomass burning emissions estimated with a global fire assimilation system based on observed fire radiative power, Biogeosciences, 9, 527–554, https://doi.org/10.5194/bg-9-527-2012, 2012.

Khanna, N., Lin, J., Liu, X., and Wang, W.: An assessment of China's methane mitigation potential and costs and uncertainties through 2060, Nat. Commun., 15, 9694, https://doi.org/10.1038/s41467-024-54038-y, 2024.

Kirschke, S., Bousquet, P., Ciais, P., Saunois, M., Canadell, J. G., Dlugokencky, E. J., Bergamaschi, P., Bergmann, D., Blake, D. R., Bruhwiler, L., and Cameron-Smith, P.: Three decades of global methane sources and sinks, Nat. Geosci., 6, 813–823, https://doi.org/10.1038/ngeo1955, 2013.

Kuze, A., Suto, H., Shiomi, K., Kawakami, S., Tanaka, M., Ueda, Y., Deguchi, A., Yoshida, J., Yamamoto, Y., Kataoka, F., Taylor, T. E., and Buijs, H. L.: Update on GOSAT TANSO-FTS performance, operations, and data products after more than 6 years in space, Atmos. Meas. Tech., 9, 2445–2461, https://doi.org/10.5194/amt-9-2445-2016, 2016.

Lai, W. and Gan, J.: On spectral nudging and dynamics to improve representation of marine cloud and precipitation over the China Sea in summer, Theor. Appl. Climatol., 156, 444, https://doi.org/10.1007/s00704-025-05689-4, 2025.

Lan, X., Thoning, K. W., and Dlugokencky, E. J.: Trends in globally-averaged CH_4, N_2O, and SF_6 determined from NOAA Global Monitoring Laboratory measurements, Version 2026-03, https://doi.org/10.15138/P8XG-AA10, 2026.

Laughner, J. L., Toon, G. C., Mendonca, J., Petri, C., Roche, S., Wunch, D., Blavier, J.-F., Griffith, D. W. T., Heikkinen, P., Keeling, R. F., Kiel, M., Kivi, R., Roehl, C. M., Stephens, B. B., Baier, B. C., Chen, H., Choi, Y., Deutscher, N. M., DiGangi, J. P., Gross, J., Herkommer, B., Jeseck, P., Laemmel, T., Lan,

https://doi.org/10.5194/egusphere-2026-3879
Preprint. Discussion started: 27 July 2026

X., McGee, E., McKain, K., Miller, J., Morino, I., Notholt, J., Ohyama, H., Pollard, D. F., Rettinger, M., Riris, H., Rousogenous, C., Sha, M. K., Shiomi, K., Strong, K., Sussmann, R., Té, Y., Velazco, V. A., Wofsy, S. C., Zhou, M., and Wennberg, P. O.: The Total Carbon Column Observing Network's GGG2020 data version, Earth Syst. Sci. Data, 16, 2197–2260, https://doi.org/10.5194/essd-16-2197-2024, 2024.

Liang, R., Zhang, Y., Chen, W., Zhang, P., Liu, J., Chen, C., Mao, H., Shen, G., Qu, Z., Chen, Z., Zhou, M., Wang, P., Parker, R. J., Boesch, H., Lorente, A., Maasakkers, J. D., and Aben, I.: East Asian methane emissions inferred from high-resolution inversions of GOSAT and TROPOMI observations: a comparative and evaluative analysis, Atmos. Chem. Phys., 23, 8039–8057, https://doi.org/10.5194/acp-23-8039-2023, 2023.

Liang, R., Zhang, Y., Hu, Q., Li, T., Li, S., Yuan, W., Xu, J., Zhao, Y., Zhang, P., Chen, W., Zhuang, M., Shen, G., and Chen, Z.: Satellite-based monitoring of methane emissions from China's rice hub, Environ. Sci. Technol., 58, 23127–23137, https://doi.org/10.1021/acs.est.4c09822, 2024.

Liu, C., Wang, W., Sun, Y., and Shan, C.: TCCON data from Hefei (PRC), Release GGG2020.R1, CaltechDATA [data set], https://doi.org/10.14291/tccon.ggg2020.hefei01.R1, 2023.

Liu, G., Peng, S., Lin, X., Ciais, P., Li, X., Xi, Y., Lu, Z., Chang, J., Saunois, M., Wu, Y., Patra, P., Chandra, N., Zeng, H., and Piao, S.: Recent slowdown of anthropogenic methane emissions in China driven by stabilized coal production, Environ. Sci. Technol. Lett., 8, 739–746, https://doi.org/10.1021/acs.estlett.1c00463, 2021.

Liu, Q., Teng, F., Nielsen, C. P., Zhang, Y., and Wu, L.: Large methane mitigation potential through prioritized closure of gas-rich coal mines, Nat. Clim. Chang., 14, 652–658, https://doi.org/10.1038/s41558-024-02004-3, 2024.

Liu, W., Li, N., Gao, P., Di, X., Liu, L., and Li, G. K.: Tracking China's methane emissions from wastewater: inventories, driving forces, and mitigation potential, Resour. Conserv. Recy., 210, 107831, https://doi.org/10.1016/j.resconrec.2024.107831, 2024.

Lorente, A., Borsdorff, T., Butz, A., Hasekamp, O., aan de Brugh, J., Schneider, A., Wu, L., Hase, F., Kivi, R., Wunch, D., Pollard, D. F., Shiomi, K., Deutscher, N. M., Velazco, V. A., Roehl, C. M., Wennberg, P. O., Warneke, T., and Landgraf, J.: Methane retrieved from TROPOMI: improvement of the data product and validation of the first 2 years of measurements, Atmos. Meas. Tech., 14, 665–684, https://doi.org/10.5194/amt-14-665-2021, 2021.

Lu, X., Jacob, D. J., Wang, H., Maasakkers, J. D., Zhang, Y., Scarpelli, T. R., Shen, L., Qu, Z., Sulprizio, M. P., Nesser, H., Bloom, A. A., Ma, S., Worden, J. R., Fan, S., Parker, R. J., Boesch, H., Gautam, R., Gordon, D., Moran, M. D., Reuland, F., Villasana, C. A. O., and Andrews, A.: Methane emissions in the United States, Canada, and Mexico: evaluation of national methane emission inventories and 2010–2017 sectoral trends by inverse analysis of in situ (GLOBALVIEWplus CH_4 ObsPack) and satellite (GOSAT) atmospheric observations, Atmos. Chem. Phys., 22, 395–418, https://doi.org/10.5194/acp-22-395-2022, 2022.

MECAP: Methane Emission Control Action Plan, https://www.mee.gov.cn/xxgk2018/xxgk/xxgk03/202311/t20231107_1055437.html, last access: 12 March 2026, 2023.

Nesser, H., Jacob, D. J., Maasakkers, J. D., Lorente, A., Chen, Z., Lu, X., Shen, L., Qu, Z., Sulprizio, M. P., Winter, M., Ma, S., Bloom, A. A., Worden, J. R., Stavins, R. N., and Randles, C. A.: High-resolution US methane emissions inferred from an inversion of 2019 TROPOMI satellite data: contributions from individual states, urban areas, and landfills, Atmos. Chem. Phys., 24, 5069–5091, https://doi.org/10.5194/acp-24-5069-2024, 2024.

Oh, Y., Bruhwiler, L., Lan, X., Schuldt, K., Basu, S., Thoning, K., Michel, S. E., Clark, R., Miller, J. B., Andrews, A., Aalto, T., Andrade, M., Aoki, S., Apadula, F., Arduini, J., Arnold, S., Baier, B., Bäni, L., Bartyzel, J., Bentz, G., Biermann, T., Biraud, S. C., Blanc, P.-E., Boenisch, H., Brailsford, G., Brand, W. A., Brunner, D., Bui, T. P. V., van den Bulk, P., Burban, B., Calzolari, F., Chang, C. S., Chen, H., Chmura, L., Choi, Y., St. Clair, J. M., Sites Climadat, Della Coletta, J., Colomb, A., Condori, L., Conen, F., Conil, S., Couret, C., Crippa, M., Cristofanelli, P., Cuevas, E., Curcoll, R., Daube, B., Davis, K. J., Dean-Day, J. M., Delmotte, M., Desai, A., DiGangi, E., Diskin, G. S., DiGangi, J. P., Elsasser, M., Emmenegger, L., Esenzhanova, G., Etiope, G., Fischer, M. L., Forster, G., Frumau, A., Fuente-Lastra, M., Fujita, R., Galkowski, M., Gatti, L. V., Gehrlein, T., Gerbig, C., Gheusi, F., Gloor, E., Goto, D., Hammer, S., Hanisco, T. F., Haszpra, L., Hatakka, J., Heimann, M., Heliasz, M., Heltai, D., Henne, S., Hensen, A., Hermans, C., Hermansen, O., Hoheisel, A., Holst, J., Di Iorio, T., Iraci, L. T., Ivakhov, V., Jaffe, D. A., Jordan, A.,

https://doi.org/10.5194/egusphere-2026-3879
Preprint. Discussion started: 27 July 2026

Joubert, W., Kang, H.-Y., Karion, A., Kazan, V., Keeling, R. F., Keronen, P., Kers, B., Kim, J., Klausen, J., Kneuer, T., Ko, M.-Y., Kolari, P., Kominkova, K., Kort, E., Kozlova, E., Krummel, P. B., Kubistin, D., Kulawik, S. S., Kumps, N., Labuschagne, C., Langenfelds, R. L., Lanza, A., Larmanou, E., Laurent, O., Laurila, T., Lauvaux, T., Lavric, J., Lee, C.-H., Lee, S., Lee, H., Lee, J., Lehner, I., Lehtinen, K., Leppert, R., Leskinen, A., Leuenberger, M., Levin, I., Levula, J., Lindauer, M., Ottosson Löfvenius, M., Loh, Z. M., Lopez, M., Lowry, D., Lueker, T. J., Lunder, C. R., Machida, T., Mammarella, I., Manca, G., Manning, A., Marek, M. V., Marklund, P., Marrero, J. E., Martin, M. Y., Martin, D., Martins, G. A., Matsueda, H., De Mazière, M., McKain, K., Meinhardt, F., Menoud, M., Metzger, J.-M., Mihalopoulos, N., Miles, N. L., Miller, C. E., Mölder, M., Monteiro, V., Montzka, S., Moore, F., Moossen, H., Moreno, C., Morgan, E., Morgui, J.-A., Morimoto, S., Müller-Williams, J., Mutuku, M., Lund Myhre, C., Necki, J., Nichol, S., Nisbet, E., Niwa, Y., Njiru, D. M., Noe, S. M., Obersteiner, F., ODoherty, S., Paramonova, N., Parworth, C. L., Peltola, O., Philippon, C., Piacentino, S., Pichon, J. M., Pickers, P., Pitt, J., Pittman, J., Plass-Dülmer, C., Platt, S. M., Popa, M. E., Pouter, B., Prinzivalli, S., Ramonet, M., Randerson, J., Richardson, S. J., Ries, L., Rigouleau, L.-J., Rivas, P. P., Röckmann, T., Rothe, M., Ryoo, J.-M., Santoni, G., di Sarra, A. G., Sasakawa, M., Scheeren, B., Schmidt, M., Schuck, T., Schumacher, M., Seifert, T., Sha, M. K., Shepson, P., Sherwood, O., Shin, D., Sloop, C. D., Smale, D., Smith, P. D., Sørensen, L. L., de Souza, R. A. F., Spain, G., Stanley, K. M., Steger, D., Steinbacher, M., Stephens, B., Sweeney, C., Taipale, R., Takatsuji, S., Thoning, K., Timas, H., Torres, G., Trisolino, P., Turnbull, J., Uhse, K., Umezawa, T., van der Veen, C., Vermeulen, A., Viner, B., Vitkova, G., de Vries, M., Watson, A., Weiss, R., van der Werf, G., Weyrauch, D., Wofsy, S. C., Worsey, J., Worthy, D., Xueref-Remy, I., Yates, E. L., Young, D., Yver-Kwok, C., Zaehle, S., Zahn, A., Zazzeri, G., Zellweger, C., Zhang, Z., and Zimnoch, M.: CarbonTracker CH_4 2025, NOAA Global Monitoring Laboratory [data set], https://doi.org/10.25925/hxks-v755, 2025.

Peng, S., Piao, S., Bousquet, P., Ciais, P., Li, B., Lin, X., Tao, S., Wang, Z., Zhang, Y., and Zhou, F.: Inventory of anthropogenic methane emissions in mainland China from 1980 to 2010, Atmos. Chem. Phys., 16, 14545–14562, https://doi.org/10.5194/acp-16-14545-2016, 2016.

Peters, W., Miller, J. B., Whitaker, J., Denning, A. S., Hirsch, A., Krol, M. C., Zupanski, D., Bruhwiler, L., and Tans, P. P.: An ensemble data assimilation system to estimate CO_2 surface fluxes from atmospheric trace gas observations, J. Geophys. Res. Atmos., 110, D24304, https://doi.org/10.1029/2005JD006157, 2005.

Peters, W., Jacobson, A. R., Sweeney, C., Andrews, A. E., Conway, T. J., Masarie, K., Miller, J. B., Bruhwiler, L. M. P., Pétron, G., Hirsch, A. I., Worthy, D. E. J., van der Werf, G. R., Randerson, J. T., Wennberg, P. O., Krol, M. C., and Tans, P. P.: An atmospheric perspective on North American carbon dioxide exchange: CarbonTracker, Proc. Natl. Acad. Sci. U.S.A., 104, 18925–18930, https://doi.org/10.1073/pnas.0708986104, 2007.

Peters, W., Krol, M. C., van der Werf, G. R., Houweling, S., Jones, C. D., Hughes, J., Schaefer, K., Masarie, K. A., Jacobson, A. R., Miller, J. B., Cho, C. H., Ramonet, M., Schmidt, M., Ciattaglia, L., Apadula, F., Heltai, D., Meinhardt, F., Di Sarra, A. G., Piacentino, S., Sferlazzo, D., Aalto, T., Hatakka, J., Ström, J., Haszpra, L., Meijer, H. A. J., van der Laan, S., Neubert, R. E. M., Jordan, A., Rodó, X., Morguí, J.-A., Vermeulen, A. T., Popa, E., Rozanski, K., Zimnoch, M., Manning, A. C., Leuenberger, M., Uglietti, C., Dolman, A. J., Ciais, P., Heimann, M., and Tans, P. P.: Seven years of recent European net terrestrial carbon dioxide exchange constrained by atmospheric observations, Glob. Change Biol., 16, 1317–1337, https://doi.org/10.1111/j.1365-2486.2009.02078.x, 2010.

Pillai, D., Buchwitz, M., Gerbig, C., Koch, T., Reuter, M., Bovensmann, H., Marshall, J., and Burrows, J. P.: Tracking city CO_2 emissions from space using a high-resolution inverse modelling approach: a case study for Berlin, Germany, Atmos. Chem. Phys., 16, 9591–9610, https://doi.org/10.5194/acp-16-9591-2016, 2016.

Qu, Z., Jacob, D. J., Shen, L., Lu, X., Zhang, Y., Scarpelli, T. R., Nesser, H., Sulprizio, M. P., Maasakkers, J. D., Bloom, A. A., Worden, J. R., Parker, R. J., and Delgado, A. L.: Global distribution of methane emissions: a comparative inverse analysis of observations from the TROPOMI and GOSAT satellite instruments, Atmos. Chem. Phys., 21, 14159–14175, https://doi.org/10.5194/acp-21-14159-2021, 2021.

Qu, Z., Jacob, D. J., Zhang, Y., Shen, L., Varon, D. J., Lu, X., Scarpelli, T., Bloom, A., Worden, J., and Parker, R. J.: Attribution of the 2020 surge in atmospheric methane by inverse analysis of GOSAT observations, Environ. Res. Lett., 17, 094003, https://doi.org/10.1088/1748-9326/ac8754, 2022.

Reum, F., Florentie, L., Peters, W., Dogniaux, M., Crevoisier, C., Sic, B., and Houweling, S.: Performance of upcoming CO2 monitoring satellites in the new high-resolution inverse model CTDAS-WRF, in: EGU General Assembly, May 2020, https://doi.org/10.5194/egusphere-egu2020-19293, 2020.

Saunois, M., Stavert, A. R., Poulter, B., Bousquet, P., Canadell, J. G., Jackson, R. B., Raymond, P. A.,

https://doi.org/10.5194/egusphere-2026-3879
Preprint. Discussion started: 27 July 2026

Dlugokencky, E. J., Houweling, S., Patra, P. K., Ciais, P., Arora, V. K., Bastviken, D., Bergamaschi, P., Blake, D. R., Brailsford, G., Bruhwiler, L., Carlson, K. M., Carrol, M., Castaldi, S., Chandra, N., Crevoisier, C., Crill, P. M., Covey, K., Curry, C. L., Etiope, G., Frankenberg, C., Gedney, N., Hegglin, M. I., Höglund-Isaksson, L., Hugelius, G., Ishizawa, M., Ito, A., Janssens-Maenhout, G., Jensen, K. M., Joos, F., Kleinen, T., Krummel, P. B., Langenfelds, R. L., Laruelle, G. G., Liu, L., Machida, T., Maksyutov, S., McDonald, K. C., McNorton, J., Miller, P. A., Melton, J. R., Morino, I., Müller, J., Murguia-Flores, F., Naik, V., Niwa, Y., Noce, S., O'Doherty, S., Parker, R. J., Peng, C., Peng, S., Peters, G. P., Prigent, C., Prinn, R., Ramonet, M., Regnier, P., Riley, W. J., Rosentreter, J. A., Segers, A., Simpson, I. J., Shi, H., Smith, S. J., Steele, L. P., Thornton, B. F., Tian, H., Tohjima, Y., Tubiello, F. N., Tsuruta, A., Viovy, N., Voulgarakis, A., Weber, T. S., van Weele, M., van der Werf, G. R., Weiss, R. F., Worthy, D., Wunch, D., Yin, Y., Yoshida, Y., Zhang, W., Zhang, Z., Zhao, Y., Zheng, B., Zhu, Q., Zhu, Q., and Zhuang, Q.: The Global Methane Budget 2000--2017, Earth Syst. Sci. Data, 12, 1561–1623, https://doi.org/10.5194/essd-12-1561-2020, 2020.

Saunois, M., Martinez, A., Poulter, B., Zhang, Z., Raymond, P. A., Regnier, P., Canadell, J. G., Jackson, R. B., Patra, P. K., Bousquet, P., Ciais, P., Dlugokencky, E. J., Lan, X., Allen, G. H., Bastviken, D., Beerling, D. J., Belikov, D. A., Blake, D. R., Castaldi, S., Crippa, M., Deemer, B. R., Dennison, F., Etiope, G., Gedney, N., Höglund-Isaksson, L., Holgerson, M. A., Hopcroft, P. O., Hugelius, G., Ito, A., Jain, A. K., Janardanan, R., Johnson, M. S., Kleinen, T., Krummel, P. B., Lauerwald, R., Li, T., Liu, X., McDonald, K. C., Melton, J. R., Mühle, J., Müller, J., Murguia-Flores, F., Niwa, Y., Noce, S., Pan, S., Parker, R. J., Peng, C., Ramonet, M., Riley, W. J., Rocher-Ros, G., Rosentreter, J. A., Sasakawa, M., Segers, A., Smith, S. J., Stanley, E. H., Thanwerdas, J., Tian, H., Tsuruta, A., Tubiello, F. N., Weber, T. S., van der Werf, G. R., Worthy, D. E. J., Xi, Y., Yoshida, Y., Zhang, W., Zheng, B., Zhu, Q., Zhu, Q., and Zhuang, Q.: Global methane budget 2000--2020, Earth Syst. Sci. Data, 17, 1873–1958, https://doi.org/10.5194/essd-17-1873-2025, 2025.

Sheng, J.-X., Jacob, D. J., Turner, A. J., Maasakkers, J. D., Sulprizio, M. P., Bloom, A. A., Andrews, A. E., and Wunch, D.: High-resolution inversion of methane emissions in the Southeast US using SEAC^{4}RS aircraft observations of atmospheric methane: anthropogenic and wetland sources, Atmos. Chem. Phys., 18, 6483–6491, https://doi.org/10.5194/acp-18-6483-2018, 2018.

Sheng, J., Song, S., Zhang, Y., Prinn, R. G., and Janssens-Maenhout, G.: Bottom-up estimates of coal

https://doi.org/10.5194/egusphere-2026-3879
Preprint. Discussion started: 27 July 2026

mine methane emissions in China: A gridded inventory, emission factors, and trends, Environ. Sci. Technol. Lett., 6, 473–478, https://doi.org/10.1021/acs.estlett.9b00294, 2019.

Skamarock, W. C. and Klemp, J. B.: A time-split nonhydrostatic atmospheric model for weather research and forecasting applications, J. Comput. Phys., 227, 3465–3485, https://doi.org/10.1016/j.jcp.2007.01.037, 2008.

Skamarock, W. C., Klemp, J. B., Dudhia, J., Gill, D. O., Liu, Z., Berner, J., Wang, W., Powers, J. G., Duda, M. G., Barker, D. M., and Huang, X.-Y.: A description of the Advanced Research WRF Version 4, NCAR Tech. Note NCAR/TN-556+STR, 145 pp., https://doi.org/10.5065/1DFH-6P97, 2019.

Soulie, A., Granier, C., Darras, S., Zilbermann, N., Doumbia, T., Guevara, M., Jalkanen, J.-P., Keita, S., Liousse, C., Crippa, M., Guizzardi, D., Hoesly, R., and Smith, S. J.: Global anthropogenic emissions (CAMS-GLOB-ANT) for the Copernicus Atmosphere Monitoring Service simulations of air quality forecasts and reanalyses, Earth Syst. Sci. Data, 16, 2261–2279, https://doi.org/10.5194/essd-16-2261-2024, 2024.

Stavert, A. R., Saunois, M., Canadell, J. G., Poulter, B., Jackson, R. B., Regnier, P., Lauerwald, R., Raymond, P. A., Allen, G. H., Patra, P. K., Bergamaschi, P., Bousquet, P., Chandra, N., Ciais, P., Gustafson, A., Ishizawa, M., Ito, A., Kleinen, T., Maksyutov, S., McNorton, J., Melton, J. R., Müller, J., Niwa, Y., Peng, S., Riley, W. J., Segers, A., Tian, H., Tsuruta, A., Yin, Y., Zhang, Z., Zheng, B., and Zhuang, Q.: Regional trends and drivers of the global methane budget, Glob. Change Biol., 28, 182–200, https://doi.org/10.1111/gcb.15901, 2022.

Steiner, M., Peters, W., Luijkx, I., Henne, S., Chen, H., Hammer, S., and Brunner, D.: European CH_4 inversions with ICON-ART coupled to the CarbonTracker Data Assimilation Shell, Atmos. Chem. Phys., 24, 2759–2782, https://doi.org/10.5194/acp-24-2759-2024, 2024.

Stocker, B. D., Roth, R., Joos, F., Spahni, R., Steinacher, M., Zaehle, S., Bouwman, L., and Prentice, I. C.: Multiple greenhouse-gas feedbacks from the land biosphere under future climate change scenarios, Nat. Clim. Chang., 3, 666–672, https://doi.org/10.1038/nclimate1864, 2013.

Sun, C., Liu, Y., Ciais, P., Broquet, G., Zheng, B., Wang, H., and Chen, H.: Measurement-based assessment reveals key drivers and mitigation potential of methane emissions from China's wastewater treatment, Sci. Adv., 12, eaec0536, https://doi.org/10.1126/sciadv.aec0536, 2026.

Takatsuji, S.: Atmospheric CH_4 at Ryori by Japan Meteorological Agency, dataset published as CH4_RYO2012_surface-insitu_JMA_data1 at WDCGG, ver. 2024-07-29-0428, World Data Centre for Greenhouse Gases (WDCGG) [data set], https://doi.org/10.50849/WDCGG_0001-2012-1002-01-01-9999, reference date: 2026/03/12, 2024a.

Takatsuji, S.: Atmospheric CH_4 at Yonagunijima by Japan Meteorological Agency, dataset published as CH4_YON2028_surface-insitu_JMA_data1 at WDCGG, ver. 2024-07-29-0428, WDCGG [data set], https://doi.org/10.50849/WDCGG_0001-2028-1002-01-01-9999, reference date: 2026/03/12, 2024b

Tewari, M., Chen, F., Wang, W., Dudhia, J., LeMone, M. A., Mitchell, K., Ek, M., Gayno, G., Wegiel, J., and Cuenca, R. H.: Implementation and verification of the unified Noah land surface model in the WRF model (formerly paper number 17.5), 20th Conference on Weather Analysis and Forecasting/16th Conference on Numerical Weather Prediction, Seattle, WA, USA, 14.2a, 14 January 2004, 2004.

Thompson, R. L., Stohl, A., Zhou, L. X., Dlugokencky, E., Fukuyama, Y., Tohjima, Y., Kim, S.-Y., Lee, H., Nisbet, E. G., Fisher, R. E., Lowry, D., Weiss, R. F., Prinn, R. G., O'Doherty, S., Young, D., and White, J. W. C.: Methane emissions in East Asia for 2000–2011 estimated using an atmospheric Bayesian inversion, J. Geophys. Res. Atmos., 120, 4352–4369, https://doi.org/10.1002/2014JD022394, 2015.

Thompson, R. L., Groot Zwaaftink, C. D., Brunner, D., Tsuruta, A., Aalto, T., Raivonen, M., Crippa, M., Solazzo, E., Guizzardi, D., Regnier, P., and Maisonnier, M.: Effects of extreme meteorological conditions in 2018 on European methane emissions estimated using atmospheric inversions, Philos. T. R. Soc. A, 380, 20200443, https://doi.org/10.1098/rsta.2020.0443, 2021.

Tohjima, Y.: Atmospheric CH_4 at Cape Ochiishi by National Institute for Environmental Studies, dataset published as CH4_COI2008_surface-insitu_NIES_data1 at WDCGG, ver. 2025-07-08-0244, WDCGG [data set], reference date: 2026/03/12, 2025a.

Tohjima, Y.: Atmospheric CH_4 at Hateruma Island by National Institute for Environmental Studies, dataset published as CH4_HAT2031_surface-insitu_NIES_data1 at WDCGG, ver. 2025-07-08-0244, WDCGG [data set], reference date: 2026/03/12, 2025b.

Tsuruta, A., Aalto, T., Backman, L., Hakkarainen, J., van der Laan-Luijkx, I. T., Krol, M. C., Spahni, R.,

https://doi.org/10.5194/egusphere-2026-3879
Preprint. Discussion started: 27 July 2026

Houweling, S., Laine, M., Dlugokencky, E., Gomez-Pelaez, A. J., van der Schoot, M., Langenfelds, R., Ellul, R., Arduini, J., Apadula, F., Gerbig, C., Feist, D. G., Kivi, R., Yoshida, Y., and Peters, W.: Global methane emission estimates for 2000–2012 from CarbonTracker Europe-CH_4 v1.0, Geosci. Model Dev., 10, 1261–1289, https://doi.org/10.5194/gmd-10-1261-2017, 2017a.

Tsuruta, A.: Application of the ensemble Kalman filter in the estimation of global methane balance, Ph.D. thesis, Department of Mathematics and Statistics, Faculty of Science, University of Helsinki, Finnish Meteorological Institute Contributions 141, FMI-CONT-141, Helsinki, Finland, 166 pp., 2017b.

Tsuruta, A., Kivimäki, E., Lindqvist, H., Karppinen, T., Backman, L., Hakkarainen, J., Schneising, O., Buchwitz, M., Lan, X., Kivi, R., Chen, H., Buschmann, M., Herkommer, B., Notholt, J., Roehl, C., Té, Y., Wunch, D., Tamminen, J., and Aalto, T.: CH4 fluxes derived from assimilation of TROPOMI XCH4 in CarbonTracker Europe-CH4: evaluation of seasonality and spatial distribution in the Northern High Latitudes, Remote Sens., 15, 1620, https://doi.org/10.3390/rs15061620, 2023.

Tsuruta, A., Kuze, A., Shiomi, K., Kataoka, F., Kikuchi, N., Aalto, T., Backman, L., Kivimäki, E., Tenkanen, M. K., McKain, K., García, O. E., Hase, F., Kivi, R., Morino, I., Ohyama, H., Pollard, D. F., Sha, M. K., Strong, K., Sussmann, R., Te, Y., Velazco, V. A., Vrekoussis, M., Warneke, T., Zhou, M., and Suto, H.: Global CH_4 fluxes derived from JAXA/GOSAT lower-tropospheric partial column data and the CarbonTracker Europe-CH_4 atmospheric inverse model, Atmos. Chem. Phys., 25, 7829–7862, https://doi.org/10.5194/acp-25-7829-2025, 2025.

Turner, A. J., Jacob, D. J., Benmergui, J., Brandman, J., White, L., and Randles, C. A.: Assessing the capability of different satellite observing configurations to resolve the distribution of methane emissions at kilometer scales, Atmos. Chem. Phys., 18, 8265–8278, https://doi.org/10.5194/acp-18-8265-2018, 2018.

van der Laan-Luijkx, I. T., van der Velde, I. R., van der Veen, E., Tsuruta, A., Stanislawska, K., Babenhauserheide, A., Zhang, H. F., Liu, Y., He, W., Chen, H., Masarie, K. A., Krol, M. C., and Peters, W.: The CarbonTracker Data Assimilation Shell (CTDAS) v1.0: implementation and global carbon balance 2001–2015, Geosci. Model Dev., 10, 2785–2800, https://doi.org/10.5194/gmd-10-2785-2017, 2017.

Vara-Vela, A. L., Karoff, C., Rojas Benavente, N., and Nascimento, J. P.: Implementation of a satellite-based tool for the quantification of CH_4 emissions over Europe (AUMIA v1.0) – Part 1: forward modelling evaluation against near-surface and satellite data, Geosci. Model Dev., 16, 6413–6431, https://doi.org/10.5194/gmd-16-6413-2023, 2023.

Wang, F., Maksyutov, S., Janardanan, R., Ito, A., Morino, I., Yoshida, Y., Someya, Y., Tohjima, Y., Kelly, B. F. J., Kaiser, J. W., Lan, X., Mammarella, I., and Matsunaga, T.: Methane emissions from Australia estimated by inverse analysis using in-situ and satellite (GOSAT) atmospheric observations, Gisci. Remote Sens., 62, 2488595, https://doi.org/10.1080/15481603.2025.2488595, 2025.

Wang, J., Ciais, P., Smith, P., Yan, X., Kuzyakov, Y., Liu, S., Li, T., and Zou, J.: The role of rice cultivation in changes in atmospheric methane concentration and the Global Methane Pledge, Glob. Change Biol., 29, 2776–2789, https://doi.org/10.1111/gcb.16631, 2023.

Wang, Y., Zhu, Z., Dong, H., Zhang, X., Wang, S., and Gu, B.: Mitigation potential of methane emissions in China's livestock sector can reach one-third by 2030 at low cost, Nat. Food, 5, 603–614, https://doi.org/10.1038/s43016-024-01010-0, 2024.

Weber, T., Wiseman, N. A., and Kock, A.: Global ocean methane emissions dominated by shallow coastal waters, Nat. Commun., 10, 4584, https://doi.org/10.1038/s41467-019-12541-7, 2019.

Wei, C., Wang, M., Fu, Q., Dai, C., Huang, R., and Bao, Q.: Temporal characteristics of greenhouse gases (CO_2 and CH_4) in the megacity Shanghai, China: association with air pollutants and meteorological conditions, Atmos. Res., 235, 104759, https://doi.org/10.1016/j.atmosres.2019.104759, 2020.

Wong, D. C., Pleim, J., Mathur, R., Binkowski, F., Otte, T., Gilliam, R., Pouliot, G., Xiu, A., Young, J. O., and Kang, D.: WRF-CMAQ two-way coupled system with aerosol feedback: software development and preliminary results, Geosci. Model Dev., 5, 299–312, https://doi.org/10.5194/gmd-5-299-2012, 2012.

Worden, J. R., Cusworth, D. H., Qu, Z., Yin, Y., Zhang, Y., Bloom, A. A., Ma, S., Byrne, B. K., Scarpelli, T., Maasakkers, J. D., Crisp, D., Duren, R., and Jacob, D. J.: The 2019 methane budget and uncertainties at 1° resolution and each country through Bayesian integration of GOSAT total column methane data and a priori inventory estimates, Atmos. Chem. Phys., 22, 6811–6841, https://doi.org/10.5194/acp-22-6811-2022, 2022.

Yang, S.-H.: Atmospheric CH_4 at Anmyeon-do by Korea Meteorological Administration, dataset

https://doi.org/10.5194/egusphere-2026-3879
Preprint. Discussion started: 27 July 2026

published as CH4_AMY2014_surface-insitu_KMA_data1 at WDCGG, ver. 2024-06-27-0750, WDCGG [data set], https://doi.org/10.50849/WDCGG_0039-2014-1002-01-01-9999, reference date: 2026/03/12, 2024a.

Yang, S.-H.: Atmospheric CH_4 at Jeju Gosan by Korea Meteorological Administration, dataset published as CH4_GSN2025_surface-insitu_KMA_data1 at WDCGG, ver. 2024-06-27-0750, WDCGG [data set], https://doi.org/10.50849/WDCGG_0039-2025-1002-01-01-9999, reference date: 2026/03/12, 2024b.

Yang, S.-H.: Atmospheric CH_4 at Ulleungdo by Korea Meteorological Administration, dataset published as CH4_ULD2159_surface-insitu_KMA_data1 at WDCGG, ver. 2024-06-27-0750, WDCGG [data set], https://doi.org/10.50849/WDCGG_0039-2159-1002-01-01-9999, reference date: 2026/03/12, 2024c.

Yin, Y., Chevallier, F., Ciais, P., Bousquet, P., Saunois, M., Zheng, B., Worden, J., Bloom, A. A., Parker, R. J., Jacob, D. J., Dlugokencky, E. J., and Frankenberg, C.: Accelerating methane growth rate from 2010 to 2017: leading contributions from the tropics and East Asia, Atmos. Chem. Phys., 21, 12631–12647, https://doi.org/10.5194/acp-21-12631-2021, 2021.

Zhang, Y., Fang, S., Chen, J., Lin, Y., Chen, Y., Liang, R., Jiang, K., Parker, R. J., Boesch, H., Steinbacher, M., Sheng, J.-X., Lu, X., Song, S., and Peng, S.: Observed changes in China's methane emissions linked to policy drivers, Proc. Natl. Acad. Sci. U.S.A., 119, e2202742119, https://doi.org/10.1073/pnas.2202742119, 2022.

Zhao, J., Chen, H., Qi, X., Chi, X., Jia, M., Jiang, F., Zhong, S., Zheng, B., and Ding, A.: Observed decade-long improvement of combustion efficiency in the Yangtze River Delta region in China, Environ. Res. Lett., 19, 074001, https://doi.org/10.1088/1748-9326/ad521e, 2024.